공학석사학위논문

수직축 풍력발전기 주위 유동에 관한 수치 해석 연구 및 자동 디플렉터를 이용한 유동 제어

Numerical study on the flow around a vertical axis wind turbine and its control using an automatic moving deflector

2019 년 2 월

서울대학교 대학원

기계항공공학부

김 형 민

Numerical study on the flow around a vertical axis wind turbine and its control using an automatic moving deflector

Hyeongmin Kim
Department of Mechanical & Aerospace Engineering
Seoul National University

Abstract

We perform large eddy simulation with an immersed boundary method to analyze the flow around a vertical axis wind turbine (VAWT). We verify the performance of a three-blade VAWT with the tip speed ratio at the Reynolds number of 80,000 based on the rotor diameter and free-stream velocity. The blades of the VAWT undergo rotational motion due to the free-stream velocity, and dynamic stall occurs as the blade's angle of attack exceeds the static stall angle. Flow separation and vortex shedding occur during dynamic stall and the blades pass through the wake from the preceding blades. In the upwind region, the power of a blade increases with increasing angle of attack, but decreases as flow separates at the leading edge of the blade and a large leading edge vortex is formed. On the other hand, the power of a blade changes mildly in the downwind region. We apply an automatic moving deflector (AMD), inspired by secondary feather of a bird's wing, to the inner surfaces of blades where flow separation occurs during dynamic stall. When flow separation occurs, the AMD pops up automatically suppressing the leading edge vortex formation. Then, the pressure distribution on the blade's surface changes and drag is

reduced. Consequently, the performance of the VAWT is enhanced at the tip speed ratios lower than 1.2.

Keywords: Vertical axis wind turbine (VAWT), dynamic stall, bio-mimetic flow control, automatic moving deflector

Student Number: 2017-24571

Contents

List of Figures

List of Tables

Nomenclature

Roman Symbols

C_D	: Drag coefficient
C_L	: Lift coefficient
C_P	: Pressure coefficient
C_{PW}	: Power coefficient
$\overline{C}_{PW}$	: Time-averaged power coefficient
$\langle C_{PW} \rangle$	: Phase-averaged power coefficient
$\langle C_{PW} \rangle_{\max}$	: Maximum phase-averaged power coefficient
c	: Chord length
D	: Diameter of rotor
F_D	: Drag
F_L	: Lift
H	: Height of blade
P	: Pressure
R	: Radius of rotor
r, t	: Radial, tangential directions
U_0	: Free-stream velocity
U_{rel}	: Relative velocity
u, v, w	: x, y, z direction velocity
u_i	: u, v, w
x, y, ,z	: Streamwise, transverse, spanwise directions
x_i	: x, y, z

Greek Symbols

α_{eff}	: Effective angle of attack
$\alpha_{\max}$	: Maximum effective angle of attack
α_{stall}	: Stall angle
β	: AMD angle
θ	: Azimuthal position
$\theta_{\max}$	: Azimuthal position when phased-averaged power is maximum
λ	: Tip speed ratio

ρ	: Density
τ	: Torque
Ω	: Rotational speed
ω_z	: Spanwise vorticity

Abbreviations

AMD	: Automatic moving deflector
HAWT	: Horizontal axis wind turbine
VAWT	: Vertical axis wind turbine

Chapter 1

Introduction

Wind turbines are classified as horizontal axis wind turbines (HAWTs) and vertical axis wind turbines (VAWTs) depending on the type of rotary shaft. HAWTs require yaw control to align the axis of rotation with the wind direction, but VAWTs rotate in a direction perpendicular to the wind direction and so they can operate regardless of the wind direction. Despite this advantage of VAWTs, HAWTs occupy most wind turbine market because the efficiency of a HAWT is higher than that of a VAWT (Pope *et al*. 2010). However, a wind farm using HAWTs needs large installation area because they should be placed far away due to wake interference (Dabiri *et al*. 2011). On the other hand, VAWTs can be placed close each other because of less wake interference, and so it was recently shown that a wind farm using VAWTs could generate more power in the same installation area (Dabiri *et al*. 2011).

Vertical axis wind turbines are divided into two types: Darrieus type and Savonius type, which are distinguished by driving force. The Darrieus-type VAWT is a lift-driven wind turbine while the Savonius-type VAWT is a drag-driven wind turbine (Islam *et al*. 2008). The Darrieus-type VAWT consists of blades, struts, and rotor. The shapes of blade and rotor are typically an airfoil and a cylinder, respectively, and struts connect the rotor to the blade. The blades are subjected to aerodynamic forces such as lift and drag by the wind, and the lift induces the rotor to rotate in the direction of rotation. On the other hand, the Savonius-type VAWT uses hollow half-cylindrical blades instead of airfoil-shaped blades, and the drag of the half-cylindrical blades induces the rotor to rotate in the direction of rotation. The Darrieus-type VAWT has higher efficiency than the Savonius-type VAWT, but it is difficult to self-start due to low starting torque (Bhutta *et al*. 2012).

The blades of the Darrieus-type VAWT undergo unsteady motions such as heaving, pitching, and surging motions due to free-stream velocity (Buchner *et al*. 2018). The blade's angle of attack changes continuously, and its maximum value exceeds the steady airfoil stall angle causing dynamic stall (Buchner *et al*. 2018). Coherent vortices are formed at the

suction surface of leading edge during dynamic stall, resulting in higher aerodynamic forces than those of the steady airfoil (Buchner *et al*. 2018; Corke *et al*. 2015). The vortices grow to the fully formed dynamic stall vortex which sheds from the blade resulting in abrupt lift drop (Buchner *et al*. 2018; Corke *et al*. 2015).

Recently, many studies have been conducted to analyze the flow characteristics and aerodynamics of the Darrieus VAWT using the experiments (Fujisawa *et al*. 1999; Ferreira *et al*. 2009; Araya *et al*. 2017; Buchner *et al*. 2018) or numerical simulations such as URANS (McLaren *et al*. 2012; Hezaveh *et al*. 2016) and LES (Posa *et al*. 2016; Ouro *et al*. 2017; Posa *et al*. 2018). Ferreira et al. (2009) showed that the vortices evolved, rolled-up and shed from the blade through PIV and that the tip speed ratio, the ratio of rotational speed to wind speed, had a significant effect on the evolution and shedding of the vortices. In addition, Buchner et al. (2018) showed that the evolution and shedding of the vortices were strongly affected by the pitching kinematics, the ratio of chord length to diameter of the rotor, as well as the tip speed ratio. Ouro *et al*. (2017) investigated the variation of aerodynamic forces according to the position of the blade and showed that the lift drop during dynamic stall occurred at a higher angle of attack than a steady airfoil.

The reason of difficult self-starting is that the lift drop during dynamic stall occurred more quickly at low tip speed ratios, and so the torque in the rotating direction could not be sufficiently generated (Hill *et al*. 2009; Tsai *et al*. 2016). Accordingly, many researches have been conducted to investigate the physics of self-starting for the Darrieus VAWT (Kirke 1998; Dominy *et al* 2007; Hill *et al* 2009; Untaroiu *et al* 2011; Tsai *et al* 2016). Kirke (1998) showed that the solidity, the ratio of the length of all blades to the circumferential length of the rotor, was one of the important factors affecting the self-starting. The VAWT with high solidity had higher starting torque than the VAWT with low solidity, which made self-starting easier. However, the performance curve of the VAWT with high solidity had a peaky shape and so the VAWT with high solidity operated over a narrow range of the tip speed ratio with lower efficiency (Kirke 1989). On the other hand, the VAWT with low solidity had low starting torque and so its tip speed ratio could not be accelerated to the operating tip speed ratio (Hill *et al* 2009; Untaroiu *et al* 2011). Therefore,

it is important for the VAWT to have high starting torque at low tip speed ratios and operate over a wide range of tip speed ratios with high efficiency.

To enhance the aerodynamic performance of the Darrieus VAWT at various tip speed ratios, several studies have been conducted on passive (Frunzulica *et al*. 2014; Wang *et al*. 2017; Sobhani *et al*. 2017) and active (Yang *et al*. 2017; Li *et al*. 2018) control devices by controlling dynamic stall in the blades of the VAWT. The active control devices achieved the performance improvement in overall tip speed ratios, but they were not practical because they required the extra energy source. Meanwhile, the passive control devices only increased the performance at limited tip speed ratios. In addition, few passive control devices can aid self-starting by enhancing the performance in low tip speed ratios.

In the present study, we investigate flow around a Darrieus VAWT and unsteady aerodynamics of blades and then suggest an automatic moving deflector (AMD), inspired by secondary feather of a bird's wing (Liebe 1979; Kim *et al*. 2016), to improve the performance of VAWT at low tip speed ratios.

Chapter 2

Numerical details

2.1. Aerodynamics and geometry of VAWT

When free-stream flows from left to right, the VAWT rotates in the counter-clockwise direction based on the aerodynamic forces of blades (Figure 2.1(a)). As the blade rotates at the speed of $R\Omega$, the free-stream velocity induces the effective angle of attack and the relative velocity (Figure 2.1(b)). The effective angle of attack and the relative velocity vary with azimuthal position, and their variations are dependent on the tip speed ratio as follows:

$$\alpha_{\text{eff}} = \tan^{-1}\left(\frac{\sin\theta}{\lambda+\cos\theta}\right),\ U_{\text{rel}} = U_0\sqrt{1+2\lambda\cos\theta+\lambda^2}\ , \tag{1}$$

where $\lambda = R\Omega/U_0$. Figure 2.2 shows the azimuthal variations of the effective angle of attack at three different tip speed ratios. The effective angle of attack exceeds the steady airfoil stall angle ($\alpha_{\text{static.stall}} \sim 10°$, Wang *et al*. 2017), and its maximum value increases as the tip speed ratio decreases. The directions of lift and drag are perpendicular and parallel to that of the relative velocity (Fig 2.1(b)). The torque is generated by the resultant force of lift and drag as follows:

$$\tau = R\left(F_L\sin\alpha_{\text{eff}} - F_D\cos\alpha_{\text{eff}}\right). \tag{2}$$

Finally, the performance of the VAWT is determined by the time-averaged power coefficient as follows:

$$\overline{C}_{PW} = \frac{1}{T}\int_0^T C_{PW}\,dt,\ C_{PW} = \frac{\tau\Omega}{\frac{1}{2}\rho U_0{}^3 DH}\ . \tag{3}$$

The geometry of VAWT is the same as the experiment of Araya *et al*. (2017) to verify our numerical results. The cross-section of the blade is the NACA0018 airfoil, and the number of blades is three. The diameter of rotor and chord length are 300 *mm* and 100 *mm*, respectively. The Reynolds number based on the diameter of rotor and free-stream velocity

is 80,000. We consider only the blades of VAWT neglecting the struts.

2.2. Governing equations

Governing equations are spatially filtered continuity and incompressible Navier-Stokes equations in Cartesian inertial coordinates:

$$\begin{aligned} &\frac{\partial \overline{u}_i}{\partial x_i} - q = 0, \\ &\frac{\partial \overline{u}_i}{\partial t} + \frac{\partial (\overline{u}_i \overline{u}_j)}{\partial x_i} = -\frac{\partial \overline{p}}{\partial x_i} + \frac{1}{\mathrm{Re}} \frac{\partial^2 \overline{u}_i}{\partial x_j \partial x_j} - \frac{\partial \tau_{ij}}{\partial x_j} + f_i, \end{aligned} \tag{4}$$

where $\tau_{ij} \equiv \overline{u_i u_j} - \overline{u}_i \overline{u}_j$ and $\overline{(\,)}$ denotes the space-filtering operation. A dynamic global model (Park *et al*. 2006; Lee *et al*. 2010) is used for the subgrid-scale stress tensor. An immersed boundary method (Kim *et al*. 2001) is used to satisfy no-slip boundary condition on the blades of a VAWT. We use a second order implicit fractional-step method (Choi *et al*. 1994) with linearization (Kim *et al*. 2002) for time advancement and a second-order central difference for spatial discretization.

In the dynamic global model (Park *et al*. 2006; Lee *et al*. 2010), the subgrid-scale stress tensor is determined as follows:

$$\begin{aligned} &\tau_{ij} = -\nu_T \left(\frac{\partial \overline{u_i}}{\partial x_j} + \frac{\partial \overline{u_j}}{\partial x_i} \right), \ \nu_T = C_v \sqrt{\frac{II_{\bar{\beta}}}{\overline{\alpha_{ij}}\,\overline{\alpha_{ij}}}}, \\ &\overline{\alpha_{ij}} = \frac{\partial \overline{u_j}}{\partial x_i}, \ II_{\bar{\beta}} = \overline{\beta_{11}}\,\overline{\beta_{22}} + \overline{\beta_{22}}\,\overline{\beta_{33}} + \overline{\beta_{33}}\,\overline{\beta_{11}} - \overline{\beta_{12}}^2 - \overline{\beta_{23}}^2 - \overline{\beta_{31}}^2, \ \overline{\beta_{ij}} = \sum_{m=1}^{3} \overline{\Delta}_m^2 \overline{\alpha_{mi}}\,\overline{\alpha_{mj}}, \\ &C_v = -\frac{1}{2} \frac{\left\langle L_{ij} M_{ij} \right\rangle_V}{\left\langle M_{ij} M_{ij} \right\rangle_V}, \ L_{ij} = \overline{u_i}\,\overline{u_j} - \overline{u_i}\,\overline{u_j}, \ M_{ij} = \sqrt{\frac{II_{\bar{\beta}}}{\overline{\alpha_{ij}}\,\overline{\alpha_{ij}}}}\,\overline{S_{ij}} - \sqrt{\frac{II_{\bar{\beta}}}{\overline{\alpha_{ij}}\,\overline{\alpha_{ij}}}}\,\overline{S_{ij}}, \end{aligned} \tag{5}$$

where ν_T is the subgrid-scale eddy viscosity, C_v is the Vreman model coefficient, and $\overline{\Delta}_m$ is the characteristic filter width in the *m*th direction, and $\overline{(\,)}$ denotes the test-filtering operation, and $\langle \bullet \rangle_V$ denotes the instantaneous volume averaging over the entire

computational domain and $\Delta / \overline{\Delta} = 2$ is assumed.

In the second order implicit fractional-step method for time advancement (Choi *et al*. 1994; Kim *et al*. 2002), the governing equations are solved as follows:

$$\frac{\hat{u}_i - u_i^n}{\Delta t} + \frac{1}{2}\left(\frac{\partial(\hat{u}_i u_j^n)}{\partial x_j} + \frac{\partial(u_i^n \hat{u}_j)}{\partial x_j} \right) = -\frac{\partial p^n}{\partial x_i} + \frac{1}{2\,\mathrm{Re}}\left(\frac{\partial^2 \hat{u}_i}{\partial x_j \partial x_j} + \frac{\partial^2 u_i^n}{\partial x_j \partial x_j} \right)$$
$$+ \frac{1}{2}\left(\frac{\partial}{\partial x_j}\left(\nu_T \frac{\partial \hat{u}_i}{\partial x_j} \right) + \frac{\partial}{\partial x_j}\left(\nu_T \frac{\partial u_i^n}{\partial x_j} \right) \right) + \frac{1}{2}\left(\frac{\partial}{\partial x_j}\left(\nu_T \frac{\partial \hat{u}_j}{\partial x_i} \right) + \frac{\partial}{\partial x_j}\left(\nu_T \frac{\partial u_j^n}{\partial x_i} \right) \right) + f_i \quad , \tag{6}$$

$$\frac{\partial^2 \phi}{\partial x_i \partial x_i} = \frac{1}{\Delta t}\left(\frac{\partial \hat{u}_i}{\partial x_i} - q \right), \tag{7}$$

$$u_i^{n+1} = \hat{u}_i - \Delta t \frac{\partial \phi}{\partial x_i}, \tag{8}$$

$$p^{n+1} = p^n + \phi - \frac{\Delta t}{2\,\mathrm{Re}} \frac{\partial^2 \phi}{\partial x_i \partial x_i}, \tag{9}$$

where $\hat{u}_i$ are the intermediate velocity components and ϕ is the pseudo-pressure. The Crank-Nicolson method is used for convection and viscous terms, and the nonlinear term is linearized (Kim *et al*. 2002) as follows:

$$u_i^{n+1} u_j^{n+1} = u_i^{n+1} u_j^n + u_i^n u_j^{n+1} - u_i^n u_j^n + O(\Delta t^2). \tag{10}$$

We determine the time interval so that the Courant-Friedrichs-Lewy (CFL) number is 2. The present method is based on a finite-volume method on a staggered mesh, and so the velocity components are defined at the cell faces and the pressure is defined at the cell center.

2.3. Computational domain and boundary conditions

Figure 2.3 shows the schematic diagram of the computational domain and boundary conditions used. The computation domain size is $-5 \le x/D \le 15$, $-10 \le y/D \le 10$, and $0 \le z/D \le 0.04$, respectively. The number of grids is 1793 (x) × 1793 (y) × 20 (z) and it is about 64 million. In the x-direction, the inflow condition is used at the inlet and the

convective condition is used at the outlet. Dirichlet condition for *u* and Neumann condition for *v* and *w* are used in the *y*-direction, and the periodic condition is used in the *z*-direction. No-slip boundary condition for the surfaces of the blades is satisfied by an immersed boundary method (Kim *et al*. 2001).

2.4. Geometry of automatic moving deflector

Figure 2.4 shows the shape of the blade with an automatic moving deflector (AMD). The pivot position, length, and thickness of the AMD are 0.3*c*, 0.2*c* and 0.01*c*, respectively. The material of the AMD is the same as that of the blade, polycarbonate-like material (3D Systems Accura® 60 Plastic, Araya *et al*. 2017). The governing equation of the AMD is Newton's second law for rotation, and 2nd order Adams-Bashforth method is used for time-advancement of the AMD as follows:

$$\begin{aligned} \ddot{\beta}^n &= \tau_{AMD}^n / I_{AMD} \\ \dot{\beta}^{n+1} &= \dot{\beta}^n + \left(\frac{3}{2}\ddot{\beta}^n - \frac{1}{2}\ddot{\beta}^{n-1} \right) \Delta t \,. \\ \beta^{n+1} &= \beta^n + \dot{\beta}^n \Delta t + \frac{1}{2}\ddot{\beta}^n \Delta t^2 \end{aligned} \tag{11}$$

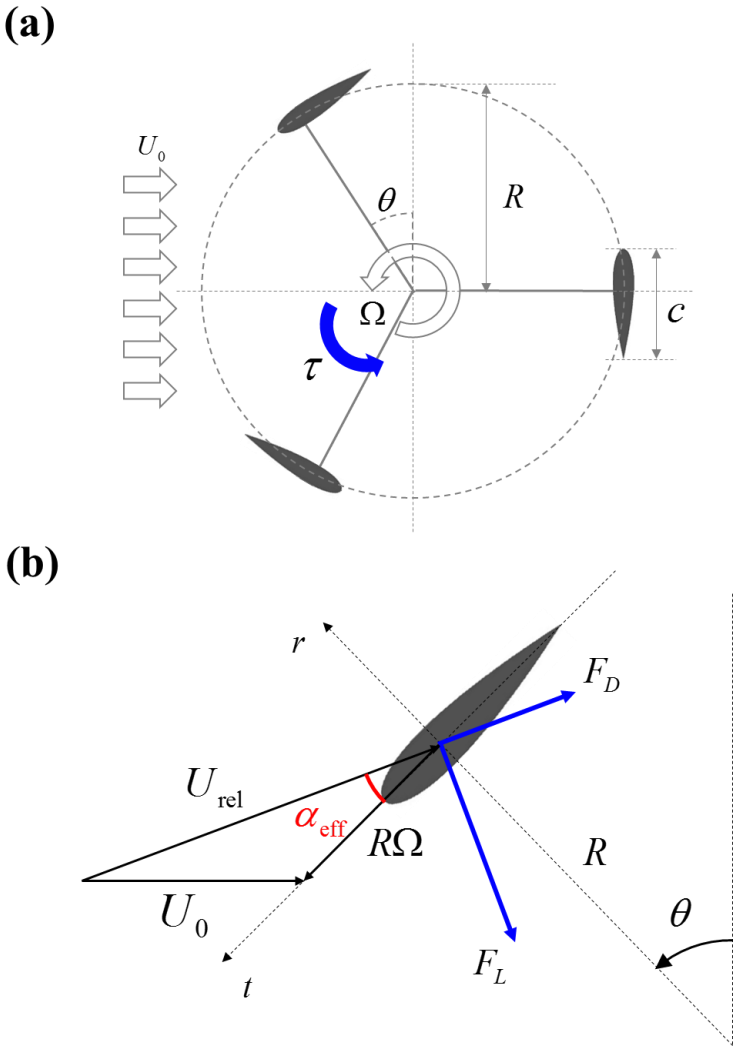

FIGURE 2.1 Schematic diagram of the VAWT: (a) overview; (b) blade.

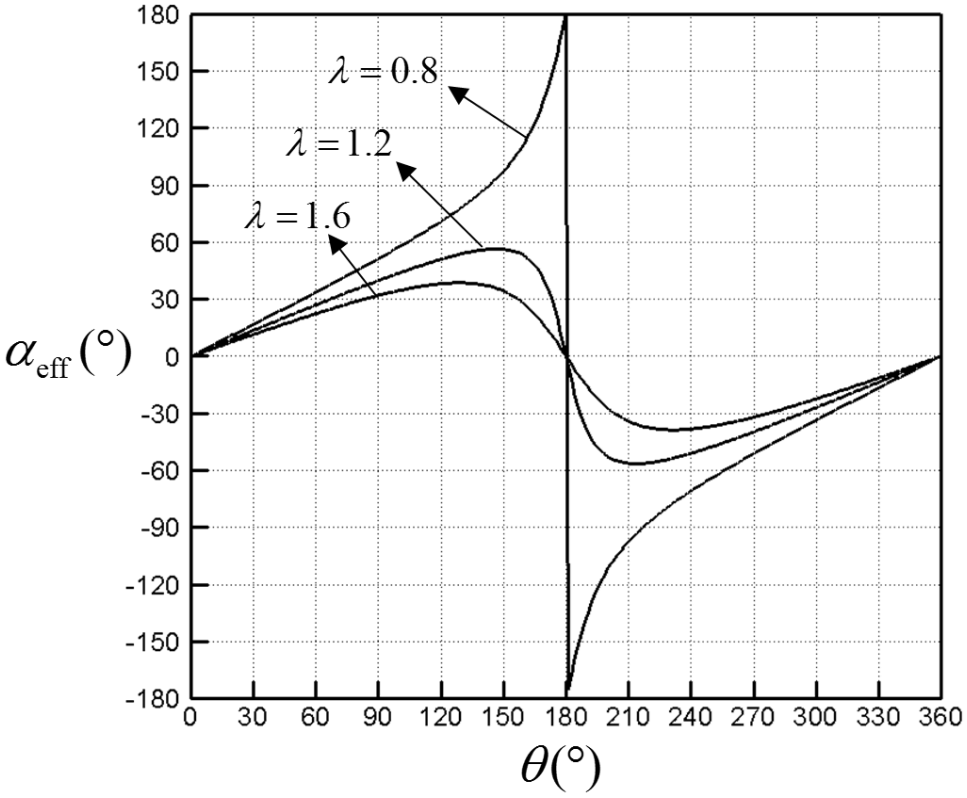

FIGURE 2.2 Azimuthal variations of the effective angle of attack at three different tip speed ratios (λ = 0.8, 1.2, 1.6).

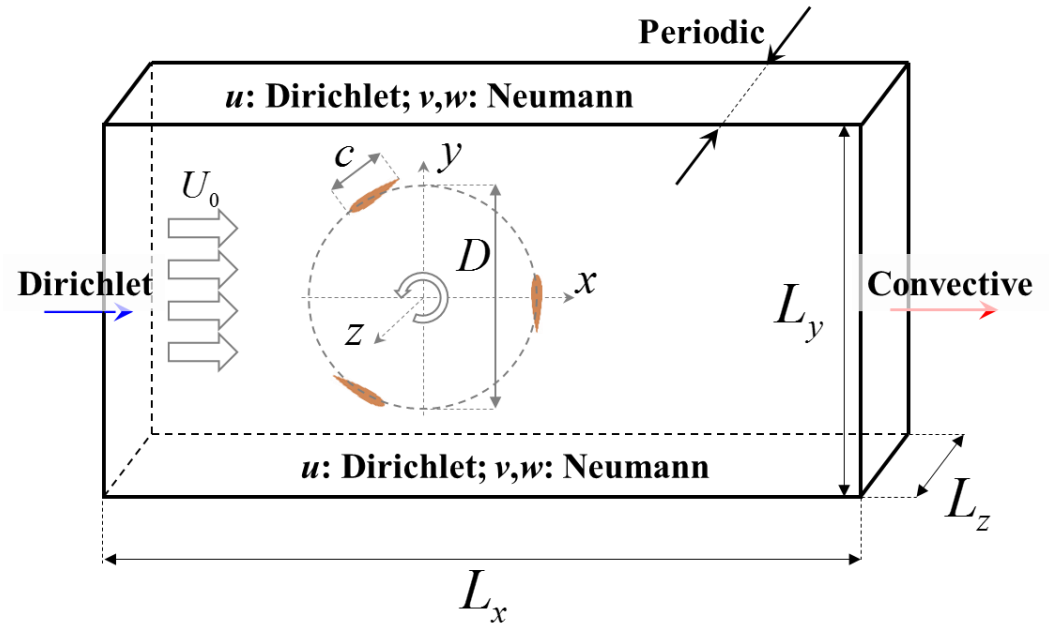

FIGURE 2.3 Schematic diagram of the computational domain and boundary conditions.

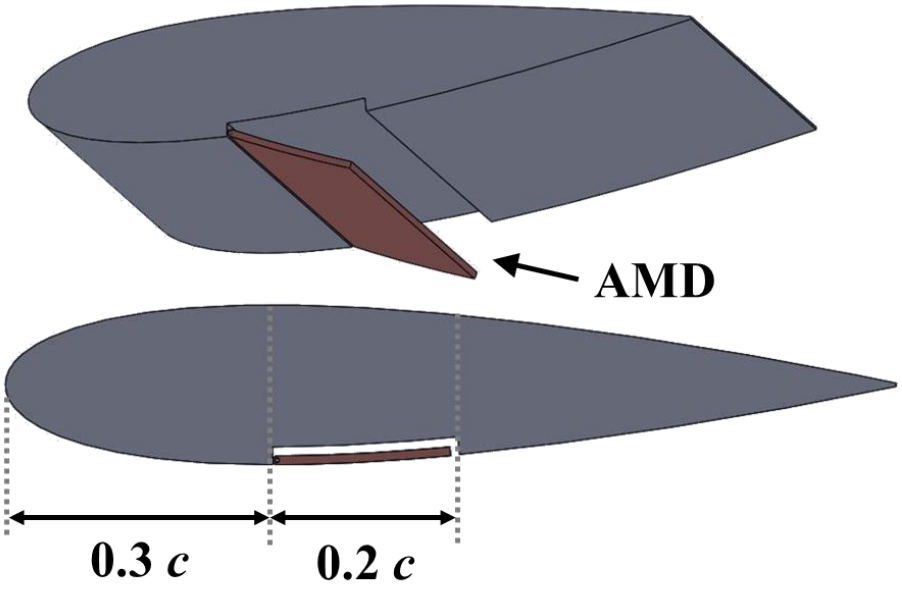

FIGURE 2.4 Schematic diagram of the AMD.

Chapter 3
Numerical Results

3.1. Performance of the VAWT

Figure 3.1 shows the change of the time-averaged power coefficient according to the tip speed ratio. Black and blue symbols indicate the experimental results from Araya *et al*. (2017) and our numerical results of the base model, respectively. The performance of VAWT is dependent on the tip speed ratio and it has a maximum value at the optimal tip speed ratio. Our numerical results show reasonable agreements at $\lambda = 1.2$ with experimental results, but there are some deviations at other tip speed ratios. This might be due to insufficient domain size and grids in the z-direction. Howell *et al*. (2010) showed that the performance of VAWT in 2-dimensional simulations was overestimated compared with that in 3-dimensional simulations. In addition, the optimal tip speed ratio is not identical in the experimental and our numerical results. The optimal tip speed ratio is about $\lambda \sim 1.2$ from the experiment results but is $\lambda = 1$ from our numerical results. This might be because we neglect the struts and only consider the blades of the VAWT. Marsh *et al*. (2015) showed that the optimal tip speed ratio changed depending on the shape and position of the strut which affected the overall performance of VAWT.

3.2. Overall flow structure

In order to investigate the flow structure at $\lambda = 1.2$ corresponding to the optimal tip speed ratio in the experiment, the contours of instantaneous spanwise vorticity are shown in figure 3.2. The direction of freestream is from left to right, and the blades are rotating in the counter-clockwise direction. As the blades rotate, various flow phenomena occur: flow separation, vortex shedding, and wake interference. In the upwind region, the flow separates at the leading edge of the blade, and then a large leading edge vortex forms and

sheds from the blade. In the downwind region, the blade passes through the wake from the preceding blade, and flow separation occurs mildly when compared to the upwind region.

To analyze the effects of the tip speed ratio on the flow structure, figure 3.3 and 3.4 show the contour of instantaneous spanwise vorticity at λ = 0.8 and 1.6, respectively. Comparing flow structure in the cases of λ = 0.8, 1.2, and 1.6, the flow separation and the formation of the leading edge vortex occur earlier in the upwind region as the tip speed ratio decreases. The leading edge vortex is observed at θ = 90° for λ = 0.8 (figure 3.3(d)), at θ = 120° for λ = 1.2 (figure 3.2(a)), and at θ = 150° for λ = 1.6 (figure 3.4(b)). This phenomenon is related to the azimuthal variation of the effective angle of attack. In figure 2.2, the effective angle of attack changes more rapidly as the tip speed ratio decreases. Accordingly, the effective angle of attack exceeds the steady airfoil stall angle earlier and so dynamic stall occurs also earlier in the upwind region.

3.3. Unsteady aerodynamics of blade

3.3.1 Variation of power

Figure 3.5 shows the azimuthal variations of phase averaged power coefficients for all blades at λ = 0.8 (red), 1.2 (black), and 1.6 (blue). The total power changes periodically, and the positive power means that the torque is generated in the rotating direction while the negative power means that the torque is generated in the counter-rotating direction. As the tip speed ratio increases, the variation range of total power increases, and the region of negative power is enlarged, and the phase of increasing power is delayed. This periodic changes in the total power affect the aerodynamic loading of the blades causing structural defects such as fatigue. However, it is necessary to analyze the aerodynamic performance of a single blade because it is difficult to analyze the changes in the flow characteristics and aerodynamic performance of the blades with the total power variation. Accordingly, figure 3.6 shows the azimuthal variations of phase averaged power coefficients for one blade at λ = 0.8 (red), 1.2 (black), and 1.6 (blue). The power increases and decreases in the upwind region, while it changes mildly in the downwind region, and the positive power is generated only in the upwind region. This means that the aerodynamic loading of the blade

changes largely in the upwind region due to free-stream velocity and so it is important to investigate the flow change with the aerodynamic forces of the blade in the upwind region.

When the power is maximum, the corresponding azimuthal position is defined as θ_{max}. Figure 3.7 shows variations of θ_{max} and maximum power with the tip speed ratio. As the tip speed ratio decreases, θ_{max} occurs earlier and the corresponding maximum value of power decreases. Accordingly, we analyze the flow characteristics by dividing the rotating region into three regions: the upwind region A (before θ_{max}), the upwind region B (after θ_{max}), and the downwind region.

3.3.2 Flow characteristics around the blade

First, we investigate the flow change at $\lambda = 1.2$ in the upwind region (figure 3.8) and the downwind region (figure 3.9), respectively. In the upwind region A ($\theta = 45^o$, 60^o, and 75^o figure 3.8(a, b, c)), the flow is almost attached on the blade, but small vortices are observed and reverse flow is induced at the trailing edge. After that, the reverse flow propagates to the leading edge and small strong vortices grow at the leading edge in the beginning of the upwind region B ($\theta = 90^o$, figure 3.8(d)). These small strong vortices grow up to a large leading edge vortex in the upwind region B ($\theta = 105^o$ and 120^o, figure 3.8(e, f)). In the beginning of the downwind region, the leading edge vortex sheds along the surface of the blade and so the blade interacts with the leading edge vortex ($\theta = 180^o$ and 210^o, figure 3.9(a, b)). After the leading edge vortex sheds from the blade, the flow separation occurs at the leading edge of the outer surface resulting in vortices shedding ($\theta = 240^o$, 270^o, 300^o, and 330^o, figure 3.9(c, d, e, f)). However, the large leading edge vortex is not observed in the downwind region compared with the upwind region. This might be because the blade passes through the wake from the preceding blade and the incident velocity on the blade is reduced due to the wake.

Next, we investigate the flow change at $\lambda = 0.8$ (figure 3.10) and 1.6 (figure 3.11) in the upwind region. Similar to the case of $\lambda = 1.2$, the flow is almost attached on the blade in the upwind region A at $\lambda = 0.8$ ($\theta = 45^o$, figure 3.10(a)) and $\lambda = 1.6$ ($\theta = 75^o$, 90^o, and 105^o,

figure 3.12(a, b, c)). In the upwind region B at λ = 0.8, the leading edge vortex grows up but its size is larger than that of λ = 1.2 (θ = 60^o, 75^o, and 90^o, figure 3.10(b, c, d)). On the other hand, the size of the leading edge vortex is reduced in the upwind region B at λ = 1.6 (θ = 120^o, 135^o, and 150^o, figure 3.11(d, e, f)). Although the timing of the leading edge vortex formation and its size are different according to the tip speed ratio, θ_{max} is nearly identical to the azimuthal position where the flow separation and the formation of leading edge vortex occur at all tip speed ratios.

3.3.3 Aerodynamic forces

In this section, we investigate aerodynamic forces of one blade such as lift and drag to understand the variation of power for one blade. Figure 3.12 shows the variations of lift (red) and drag (blue) coefficients with the effective angle of attack at λ = 1.2, and α_{stall} is defined as the effective angle of attack corresponding to θ_{max} in figure 2.2. In the upwind region A, lift and drag increases with the effective angle of attack. Lift increases faster than drag and so the torque increases. After the effective angle of attack exceeds α_{stall}, lift decreases faster than drag although the effective angle of attack increases in the beginning of the upwind region B. As the effective angle of attack returns to 0 degree, lift is negative causing the counter-rotational torque and negative drag goes to zero. In the downwind region, the effective angle of attack is negative and so the negative value of lift induces the rotational torque, but the positive value of drag induces the counter-rotational torque. The absolute value of lift is slightly larger than that of drag, but the direction of drag is close to the tangential direction and so the resultant torque is generated in the counter-rotational direction.

Figure 3.13 shows the variations of lift (red) and drag (blue) coefficients with the effective angle of attack at λ = 0.8. Similar to the case of λ = 1.2, lift increases faster than drag with the effective angle of attack in the upwind region A. After the effective angle of attack exceeds α_{stall}, lift decreases but drag still increases for a while and then decreases. Lift and drag increase with the effective angle of attack again in the end of the upwind

region B. Positive lift still induces the rotational torque, but the negative value of drag induces the counter-rotational torque over $\alpha_{eff} = 90^{o}$ and so the resultant torque is generated in the counter-rotational direction. In the downwind region, the variations of lift and drag are larger than those of $\lambda = 1.2$, which might be that the blade undergoes less wake interference due to the low rotational speed. Figure 3.14 shows the variations of lift (red) and drag (blue) coefficients with the effective angle of attack at $\lambda = 1.6$. In the upwind region, the variations of lift and drag are very similar to those of $\lambda = 1.2$, but they are smaller than those of $\lambda = 1.2$ in the downwind region. As the tip speed ratio increases, the variations of lift and drag decreases in the downwind region, which means that the wake interference between the blades is more significant at higher tip speed ratios.

In the previous results, we can know that lift decreases as the effective angle of attack increases over the stall angle, which is called dynamic stall. In addition, the effective angle of attack increases faster as the tip speed ratio decreases, and so dynamic stall occur earlier at lower tip speed ratios. In order to understand the timing of dynamic stall, variations of the maximum effective angle of attack and stall angle are shown in figure 3.15. The maximum effective angle of attack decreases as the tip speed ratio increase, but the stall angle is almost the same regardless of the tip speed ratio. Therefore, in the upwind region, the power is maximum when the effective angle of attack reaches stall angle which is nearly independent on the tip speed ratio.

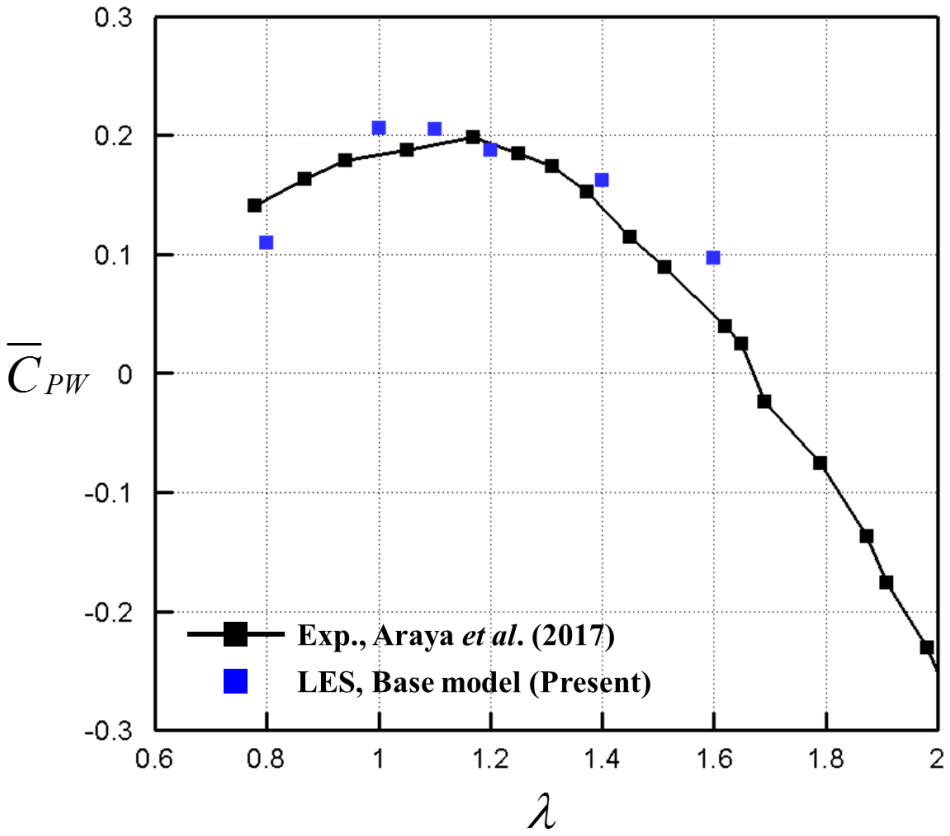

FIGURE 3.1 Performance of the VAWT with the tip speed ratio.

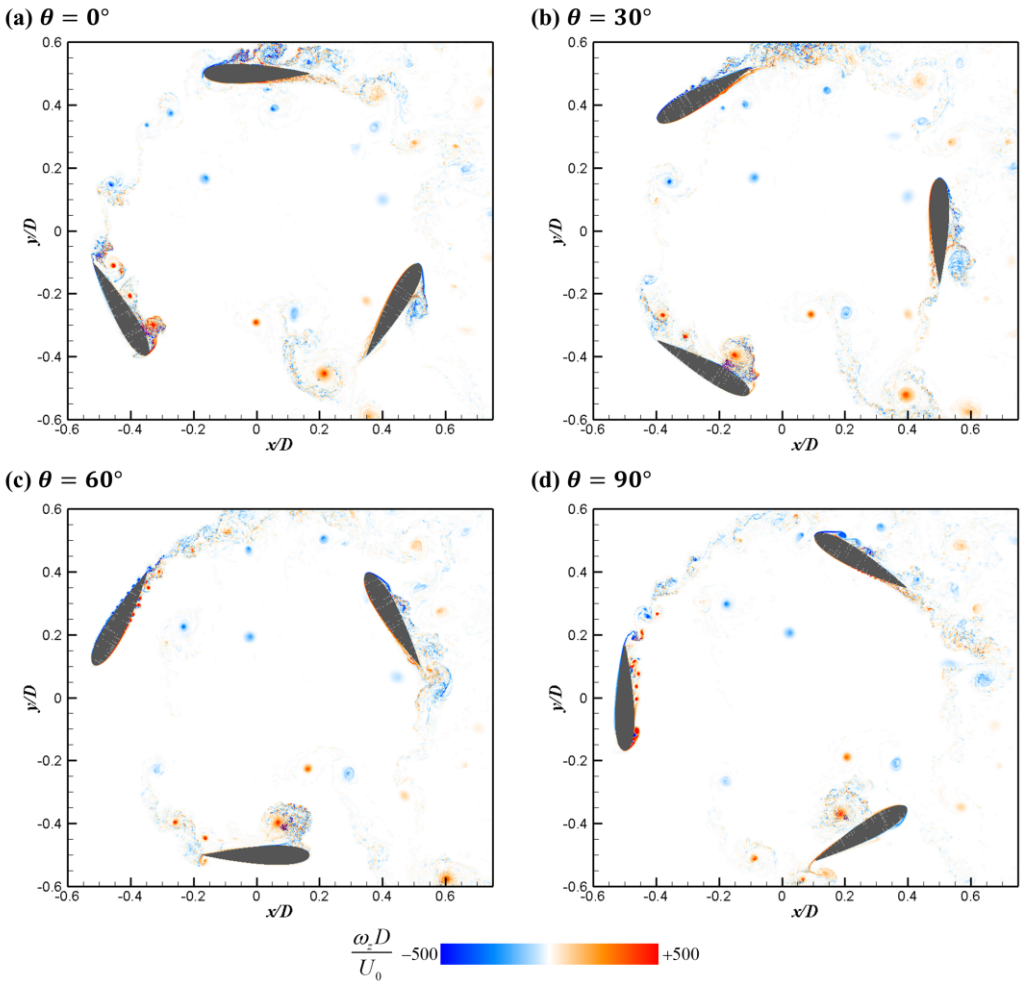

FIGURE 3.2 Contours of the instantaneous spanwise vorticity at λ = 1.2: (a) θ = 0°; (b) θ = 30°; (c) θ = 60°; (d) θ = 90°.

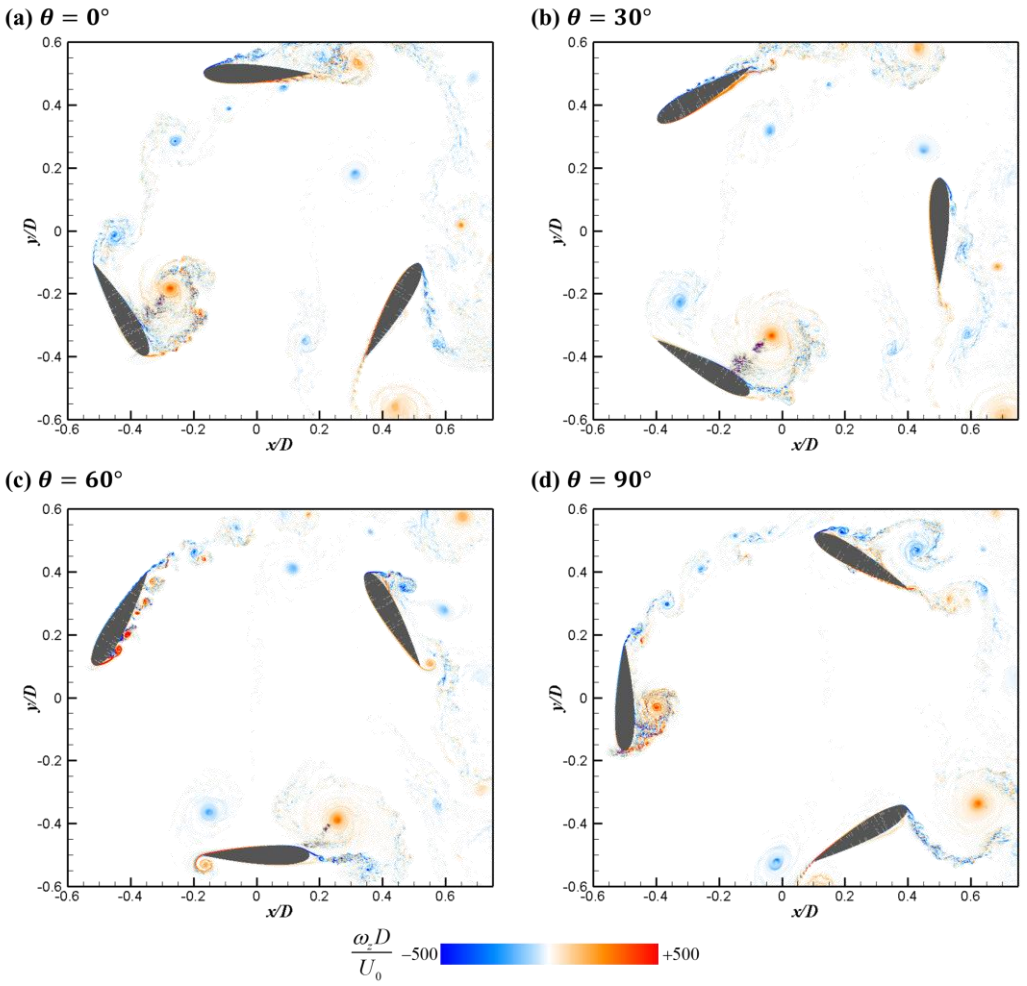

FIGURE 3.3 Contours of the instantaneous spanwise vorticity at λ = 0.8: (a) θ = 0°; (b) θ = 30°; (c) θ = 60°; (d) θ = 90°.

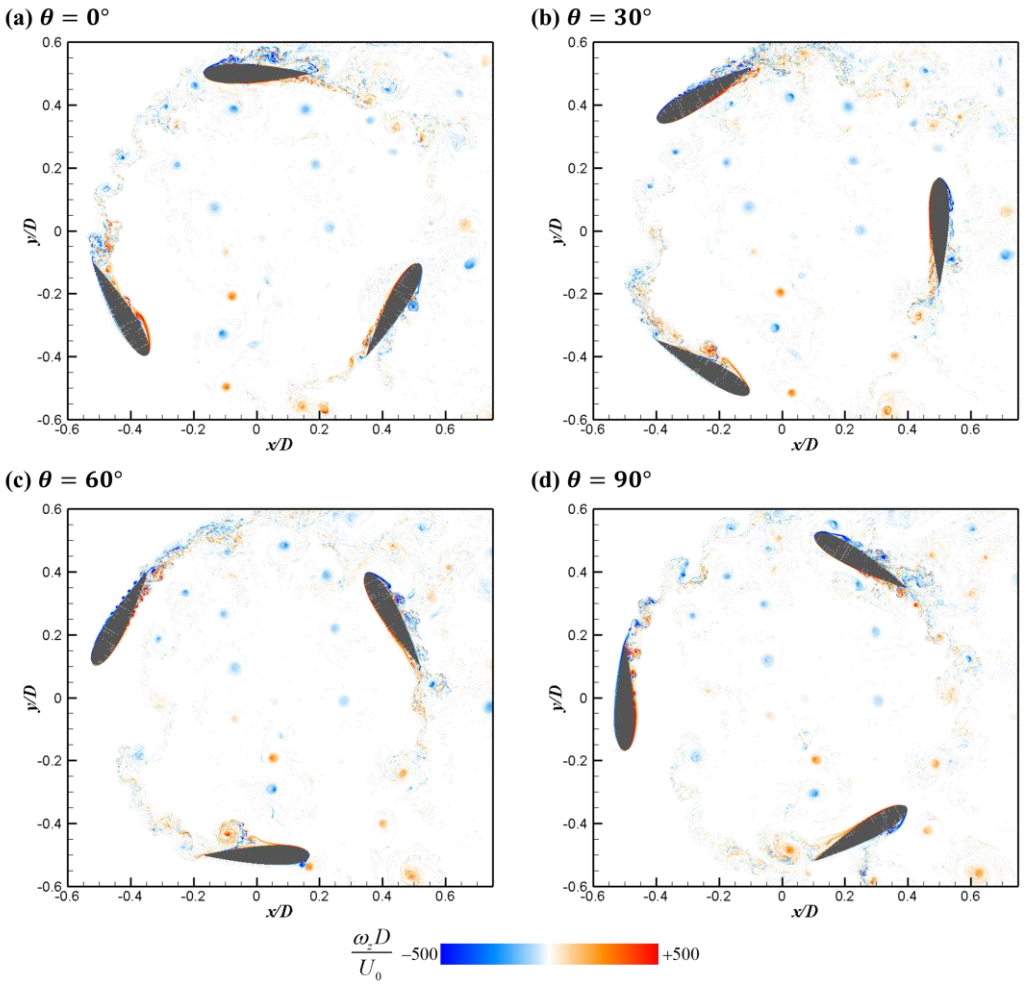

FIGURE 3.4 Contours of the instantaneous spanwise vorticity at λ = 1.6: (a) θ = 0°; (b) θ = 30°; (c) θ = 60°; (d) θ = 90°.

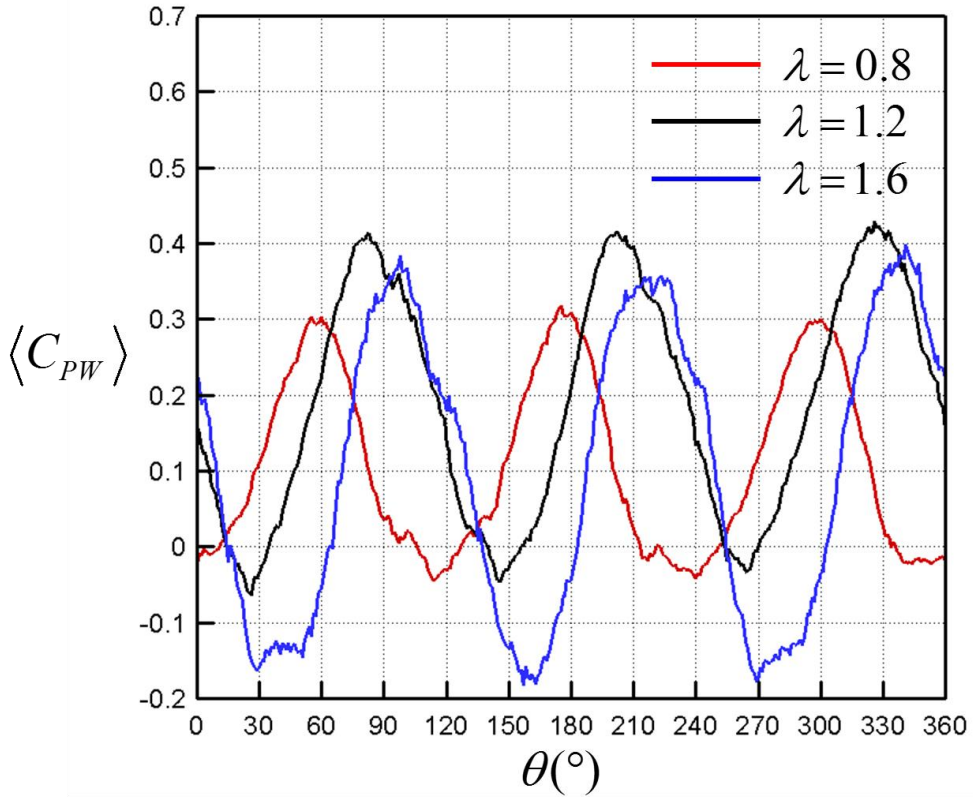

FIGURE 3.5 Azimuthal variations of phase-averaged power coefficients for all blades at λ = 0.8 (red), 1.2 (black), and 1.6 (blue).

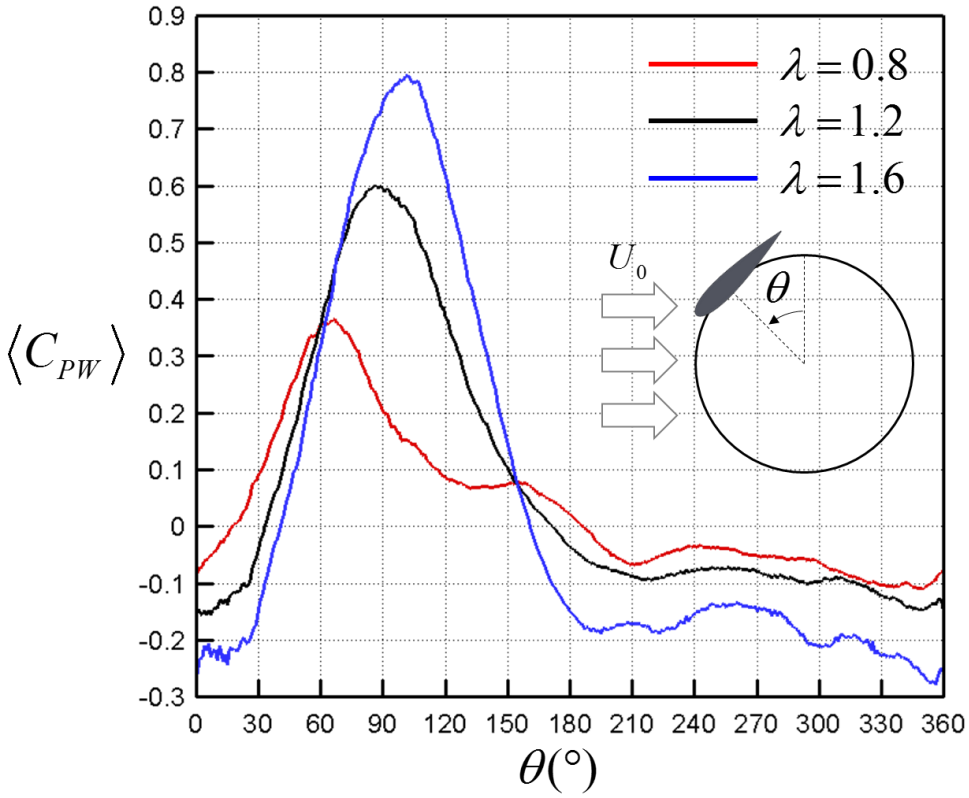

FIGURE 3.6 Azimuthal variations of phase-averaged power coefficients for one blade at λ = 0.8 (red), 1.2 (black), and 1.6 (blue).

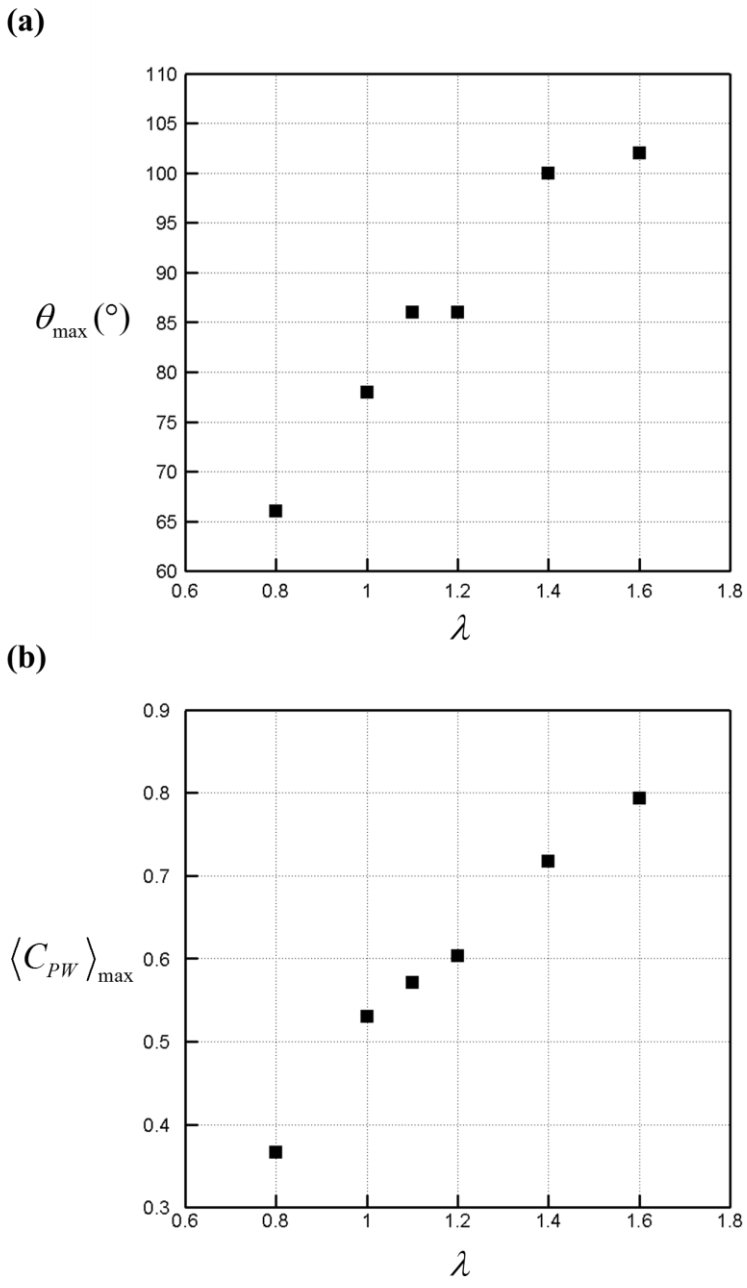

FIGURE 3.7 Variations of $\theta_{\max}$ and maximum power with the tip speed ratio.

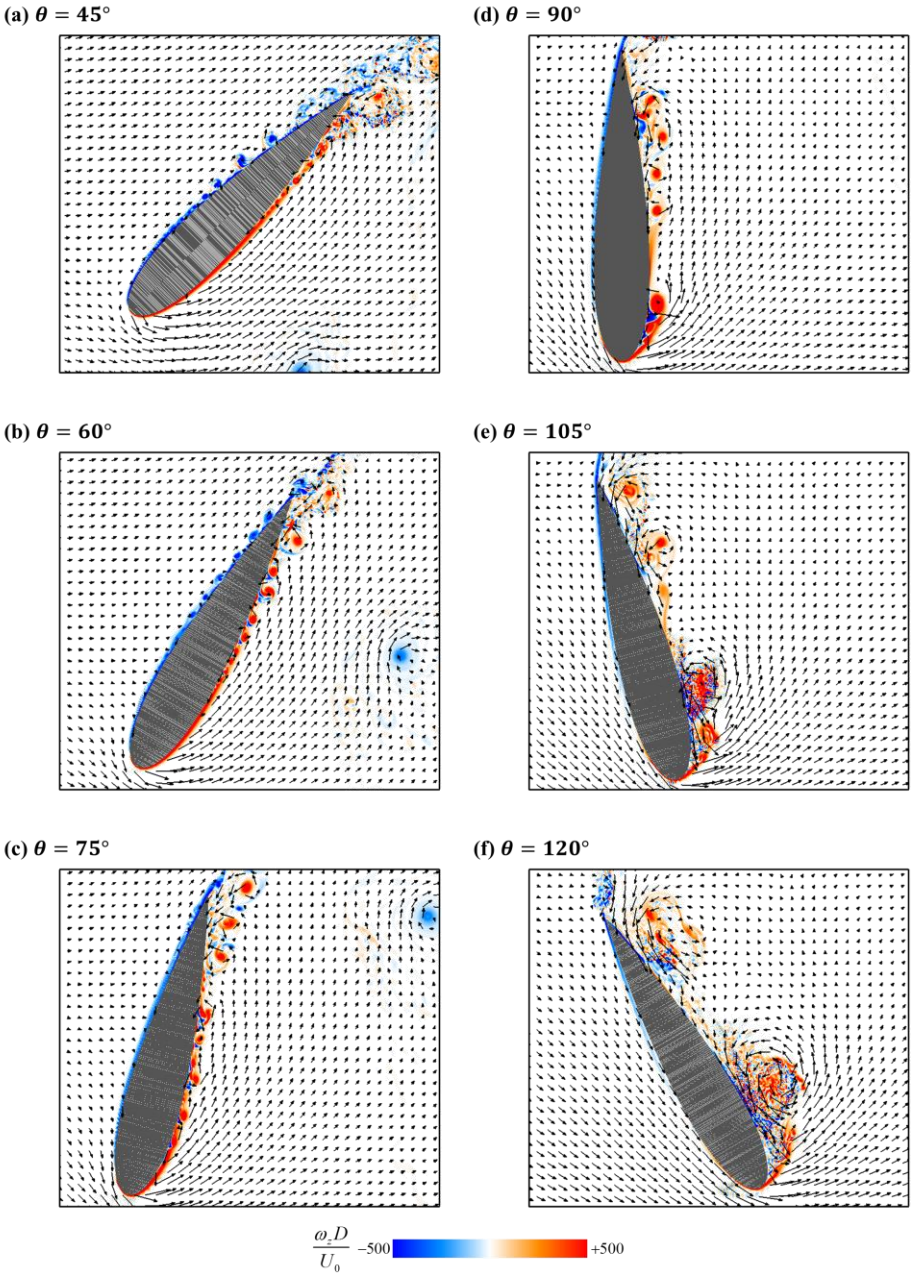

FIGURE 3.8 Instantaneous spanwise vorticity contours and velocity vectors around the blade in the upwind region at λ = 1.2: (a) θ = 45°; (b) θ = 60°; (c) θ = 75°; (d) θ = 90°; (e) θ = 105°; (f) θ = 120°.

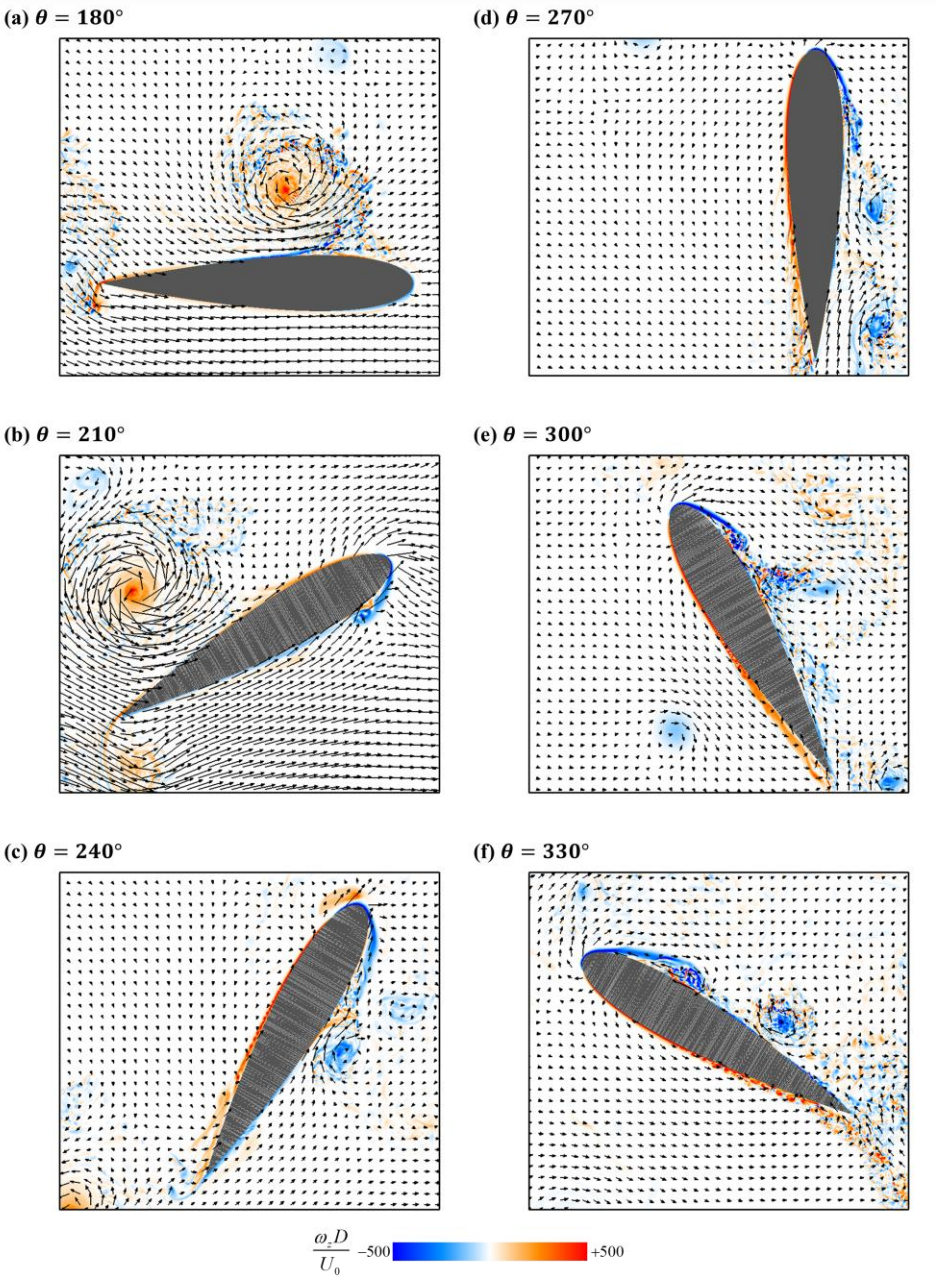

FIGURE 3.9 Instantaneous spanwise vorticity contours and velocity vectors around the blade in the downwind region at λ = 1.2: (a) θ = 180°; (b) θ = 210°; (c) θ = 240°; (d) θ = 270°; (e) θ = 300°; (f) θ = 330°.

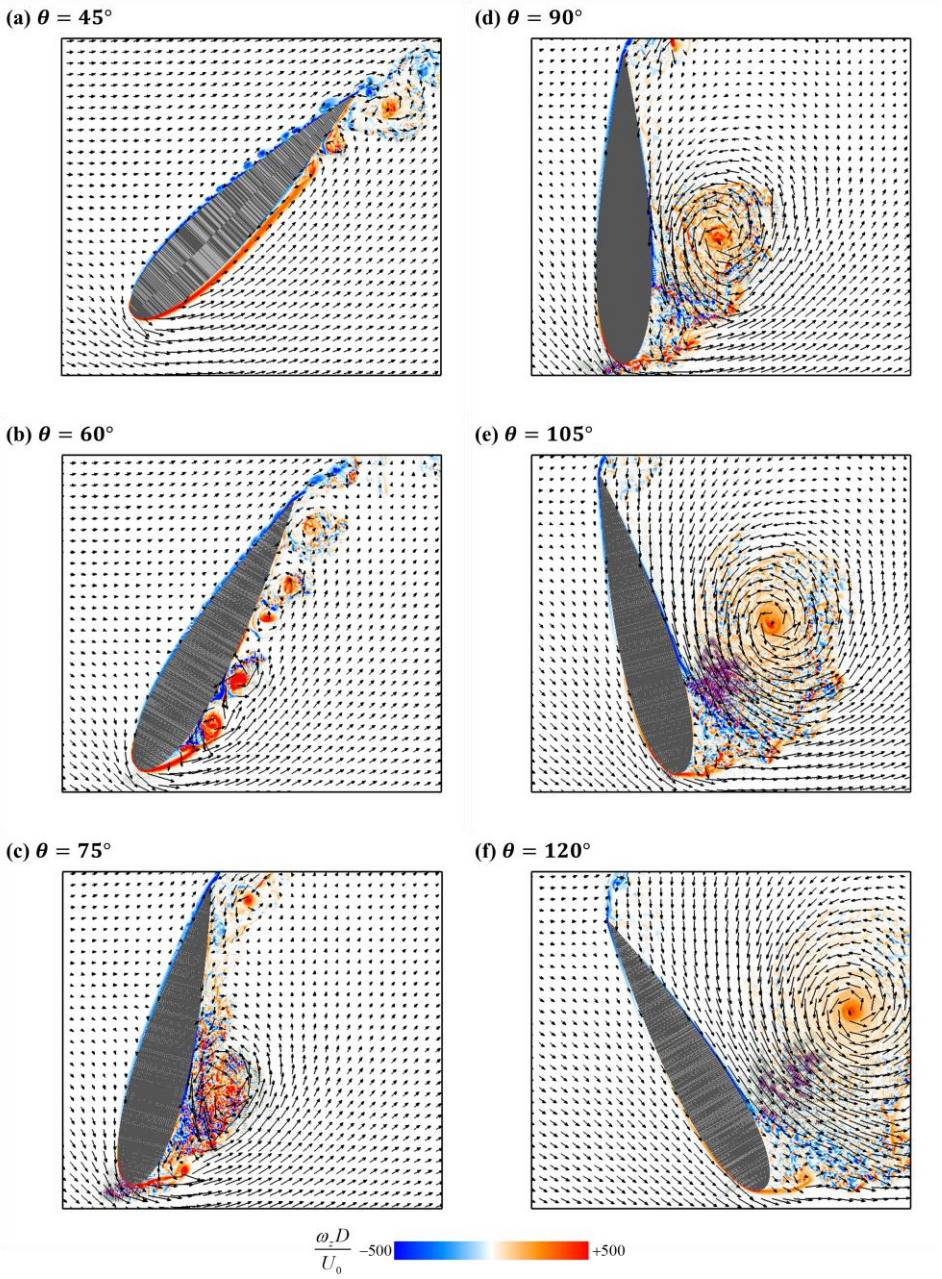

FIGURE 3.10 Instantaneous spanwise vorticity contours and velocity vectors around the blade in the upwind region at λ = 0.8: (a) θ = 45°; (b) θ = 60°; (c) θ = 75°; (d) θ = 90°; (e) θ = 105°; (f) θ = 120°.

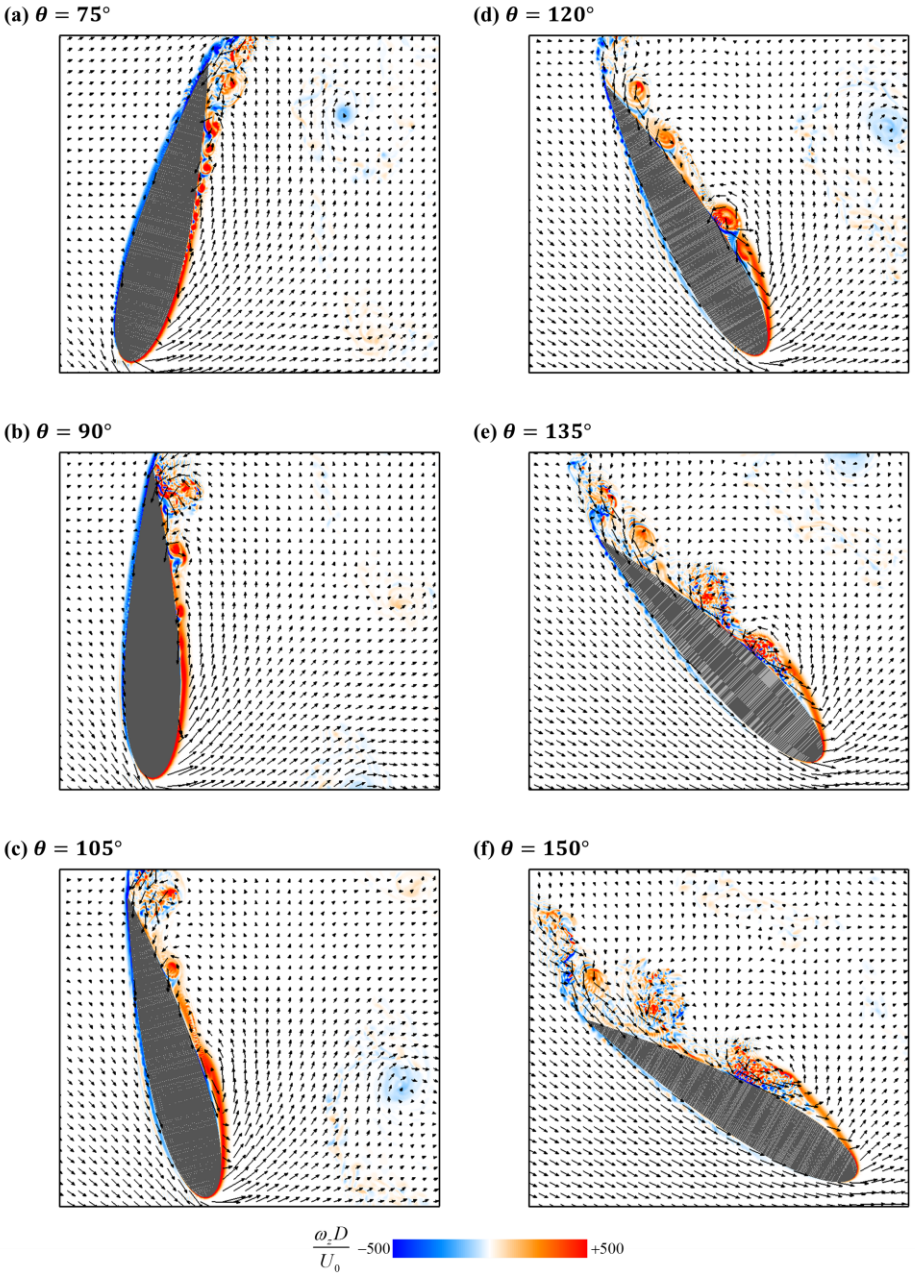

FIGURE 3.11 Instantaneous spanwise vorticity contours and velocity vectors around the blade in the upwind region at λ = 1.6: (a) θ = 75°; (b) θ = 90°; (c) θ = 105°; (d) θ = 120°; (e) θ = 135°; (f) θ = 150°.

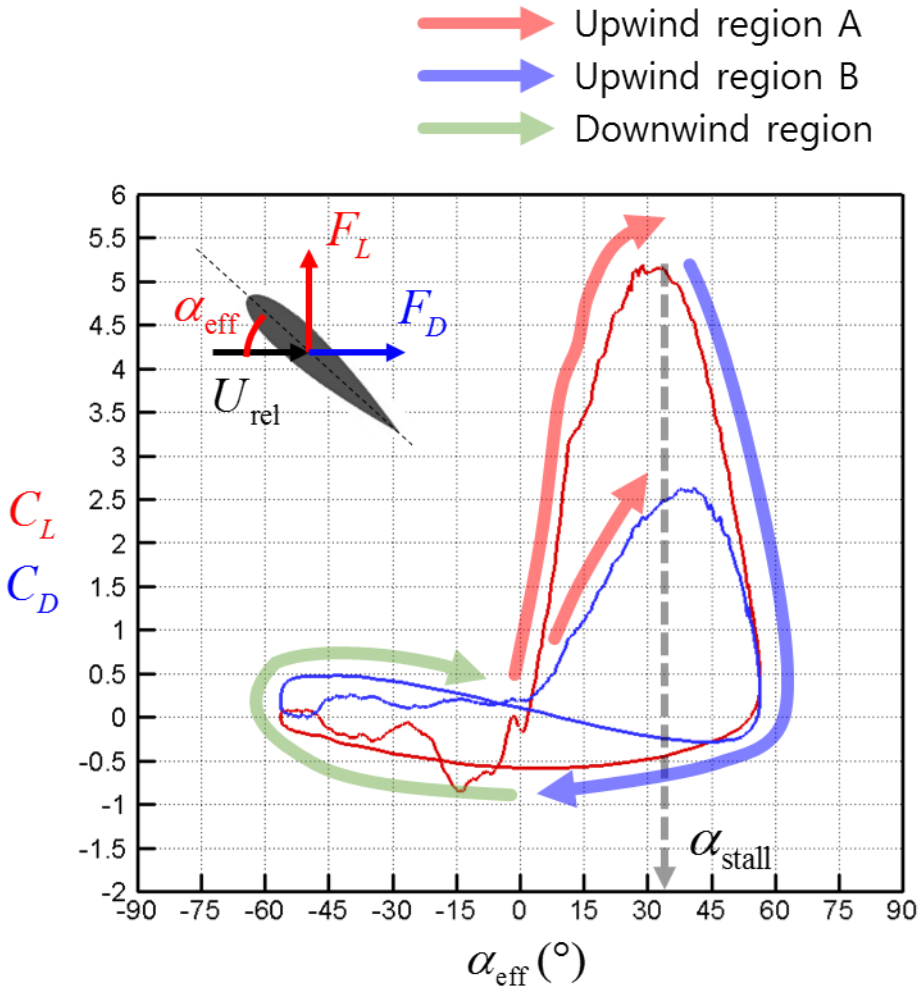

FIGURE 3.12 Variations of lift (red) and drag (blue) coefficients with the effective angle of attack at λ = 1.2.

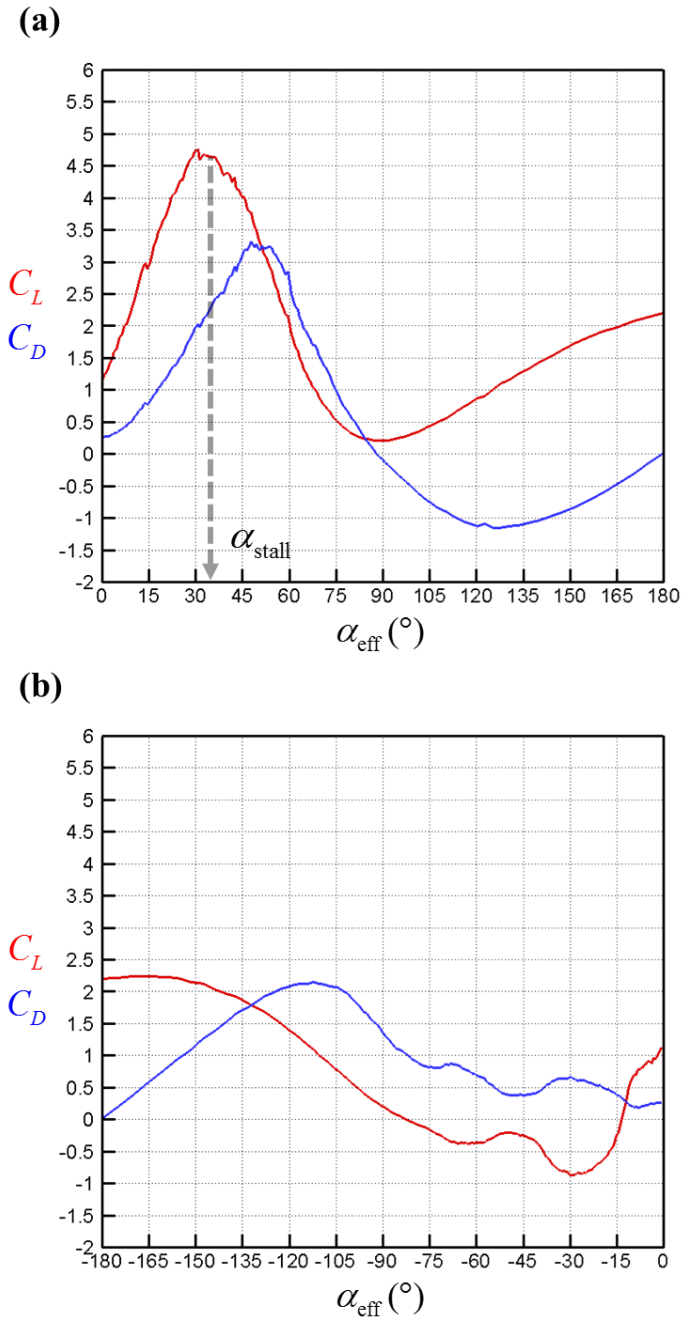

FIGURE 3.13 Variations of lift (red) and drag (blue) coefficients with the effective angle of attack at λ = 0.8: (a) upwind region; (b) downwind region.

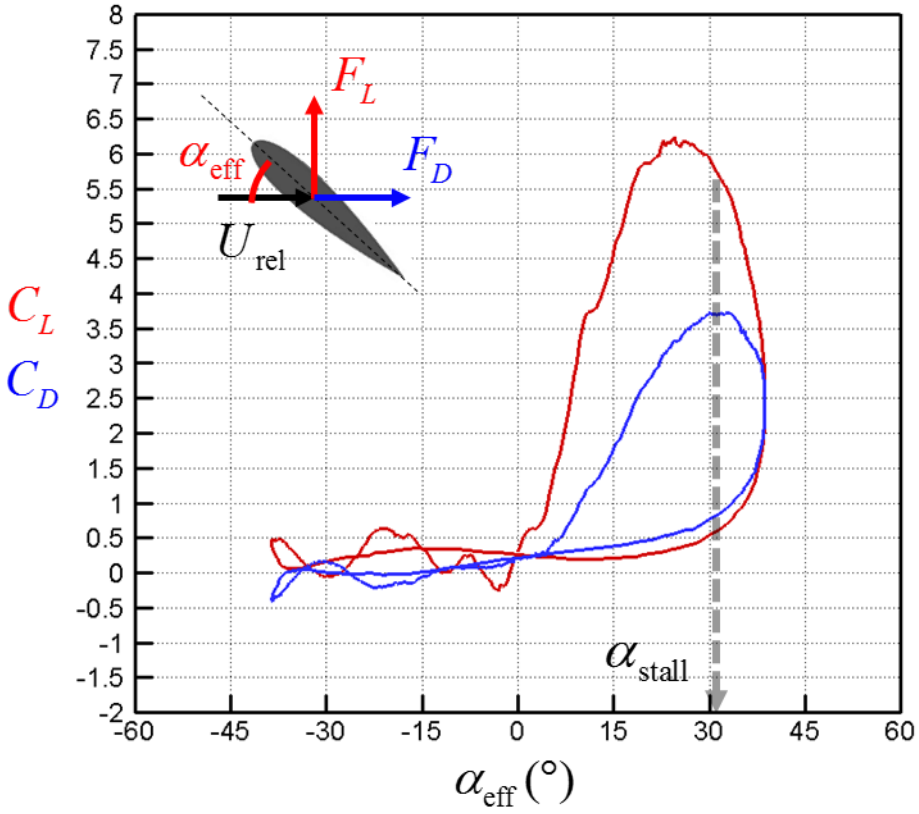

FIGURE 3.14 Variations of lift (red) and drag (blue) coefficients with the effective angle of attack at λ = 1.6.

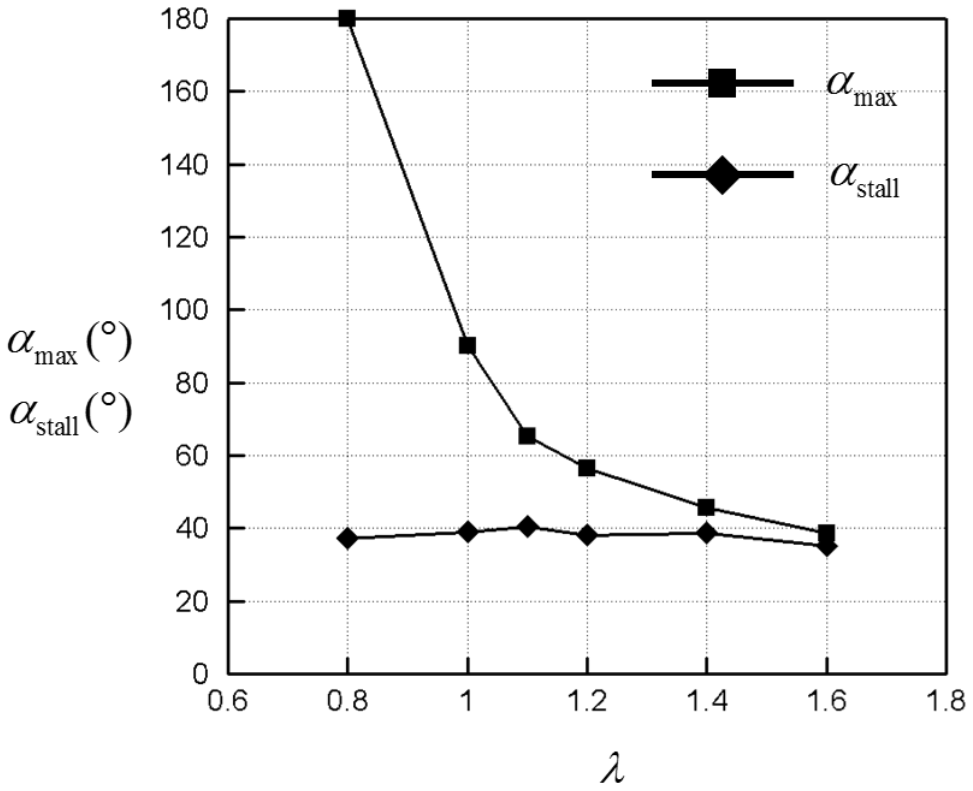

FIGURE 3.15 Variations of the maximum effective angle of attack and stall angle with the tip speed ratio.

Chapter 4

Flow control

4.1. Introduction about an automatic moving deflector

In the previous chapter, we know that dynamic stall occurs as the effective angle of attack exceeds the stall angle which is very high. In order to enhance the aerodynamic performance during dynamic stall, we applied an automatic moving deflector, inspired by the secondary feather of a bird's wing (Liebe 1979; Bechert *et al*. 1997), to the blades (figure 2.4). When a bird is landing, a secondary feather pops up (figure 4.1(a)). Liebe (1979) explained that this behavior was to enhance lift at high angles of attack, and so several studies applied it to an airfoil to obtain high lift at high angles of attack (Bechert *et al*. 1997; Meyer *et al*. 2007; Kernstine *et al*. 2008; Wang *et al*. 2012) and named it as the self-activated movable flap. When the flow is attached around the airfoil at low angles of attack, the flap is attached on the blade (figure 4.1(b) - left). However, the flow separation occurs at high angles of attack and reverse flow induces the flap to pop up automatically (figure 4.1(b) - right). As a result, the flow remains attached at higher angles of attack obtaining higher lift.

Furthermore, this concept was even applied to the model vehicle to reduce drag named as an automatic moving deflector (AMD) by Kim *et al*. (2016). In the mean flow fields at the rear of the model vehicle, the flow separates at the front edge of the slanted surface and separation bubble is formed causing the pressure drop at the slanted surface. The AMD pops up automatically from the slanted surface due to recirculating flow. With the AMD, the flow remains attached to its upper surface resulting in pressure recovery on the slanted surface and so drag reduction is achieved.

In the case of the VAWT, the flow separation occurs at high angles of attack, which affects the unsteady aerodynamics of the blade significantly. Therefore, we applied the AMD to the inner surfaces of the blade to suppress the flow separation.

4.2. Control result

We simulate the three tip speed ratio condition: λ = 0.8, 1, and 1.2, and the performance of the AMD model is shown in figure 4.2. The rate of change in the performance of the VAWT is shown in Table 4.1. The performance of the AMD model is reduced slightly at λ = 1.2, but it is enhanced largely at λ = 0.8 and 1. Self-starting of the VAWT can be aided by enhancing the performance at low tip speed ratios because the VAWT has low starting torque at low tip speed ratios (Hill *et al*. 2009; Untaroiu *et al*. 2011).

TABLE 4.1 Rate of change in the performance of the VAWT.

Tip speed ratio (λ)		0.8	1	1.2
$\overline{C}_{PW}$	Base model	0.1095	0.2063	0.1881
	AMD model	0.1676	0.2251	0.1819
$\Delta(\%) = \frac{\overline{C}_{PW.\mathrm{AMD}} - \overline{C}_{PW.\mathrm{Base}}}{\overline{C}_{PW.\mathrm{Base}}} \times 100$		+ 53.06	+ 9.11	- 3.30

In order to understand the performance enhancement at low tip speed ratios, the azimuthal variations of the power for one blade and the AMD angle are shown in figure 4.3. Black and red lines indicate the phase-averaged power coefficient of the base model and the AMD model, respectively, and blue line indicates the AMD angle. The AMD opens slowly at the beginning of the upwind region (θ = 30°, 60 °, figure 4.4(b, c)), and then it pops up rapidly while flow separates at the leading edge and the leading edge vortex forms (θ = 90°, figure 4.4(d)). After leading edge vortex sheds from the blade, the AMD closes rapidly (θ = 180°, 210 °, figure 4.4(c, d)), and then it remains closed in the downwind region. When the AMD pops up and remains open, the power of the AMD model decreases more slowly than that of the base model and so the positive power is more generated. Although the small loss of power occurs while the AMD is closing, the amount of increased power

is greater than that of decreased power resulting in the time-averaged power coefficient enhanced.

Figure 4.5 shows the variations of aerodynamic forces according to the effective angle of attack in the upwind region. Solid and dashed lines indicate the aerodynamic forces of the base model and the AMD model, respectively. As the effective angle of attack increases, the lift of the base model increases faster than that of the AMD model and so the power is slightly decreased. However, after the effective angle of attack exceeds the stall angle, drag of the AMD model is reduced largely compared with that of the base model from $\alpha_{eff} = 45^{o}$ to $\alpha_{eff} = 60^{o}$, and this period is correspondent to the period in which the power is increased by the AMD. This means that drag reduction can be achieved during dynamic stall by applying the AMD to the blade.

Accordingly, the flow fields of the base model and the AMD model are compared during the period in which the drag reduction is achieved in figure 4.6. At the beginning of the upwind region, the AMD starts to pop up due to the recirculating flow induced by small vortices (figure 4.6(a, b, c, d)). The opened AMD obstructs the spread of flow separation from the trailing edge to the leading edge and suppresses the formation of the leading edge vortex (figure 4.6 (e, f)). Consequently, the size of leading edge vortex is reduced in the AMD model, and then the shedding of leading edge vortex from the blade is delayed (figure 4.6 (g, h)). The change in pressure distribution on the blade surface by suppressing the formation of leading edge vortex at $\theta = 90^{o}$ is shown in Figure 4.7, and the pressure is averaged in the spanwise direction. In the case of the base model, the leading edge vortex is shedding from the blade and its location is around the center of the blade and so the low pressure region is located at the center of the blade's inner surface. In the case of the AMD model, the leading edge vortex is suppressed at the leading edge and located at the front of the AMD. As a result, the low pressure region is located at the front of the blade's inner surface and the low pressure at the center of the blade's inner surface is recovered to the pressure of the trailing edge. In addition, the pressure difference between the inner and outer surfaces of the AMD is made and so the additional torque in the rotational direction is induced.

(a)

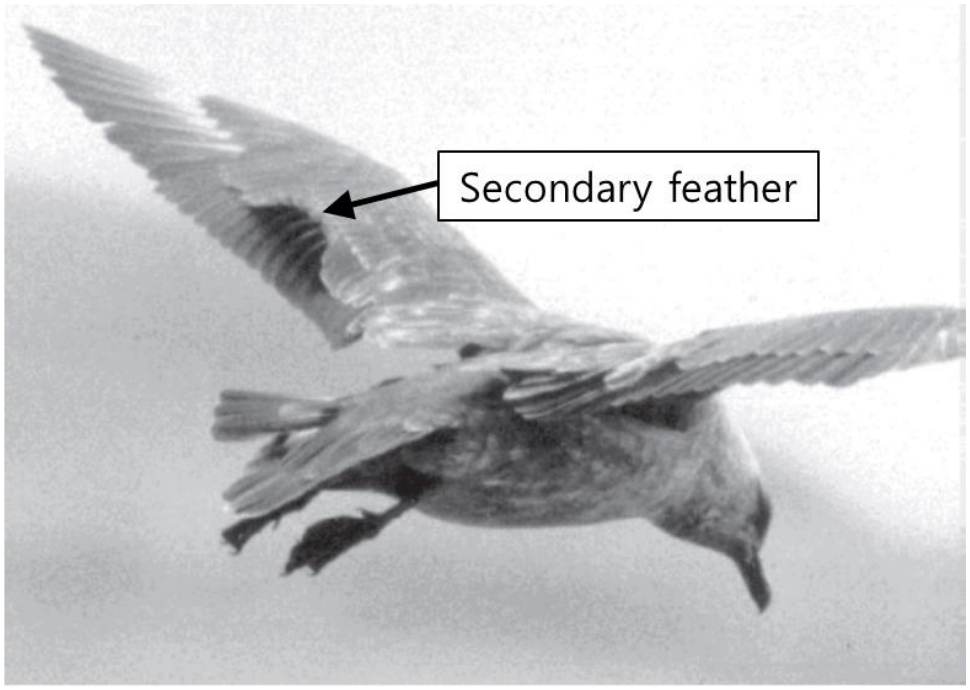

(b)

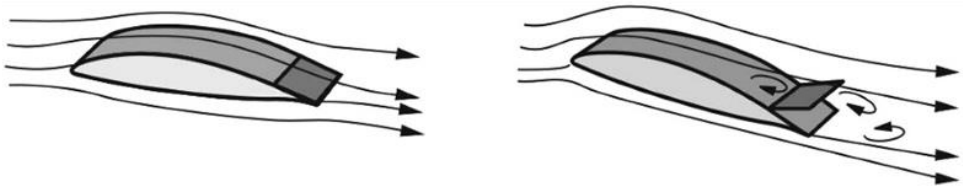

FIGURE 4.1 (a) Secondary feather of a bird's wing (photo by I. Rechenberg); (b) self-activated movable flap (Meyer *et al*. 2007).

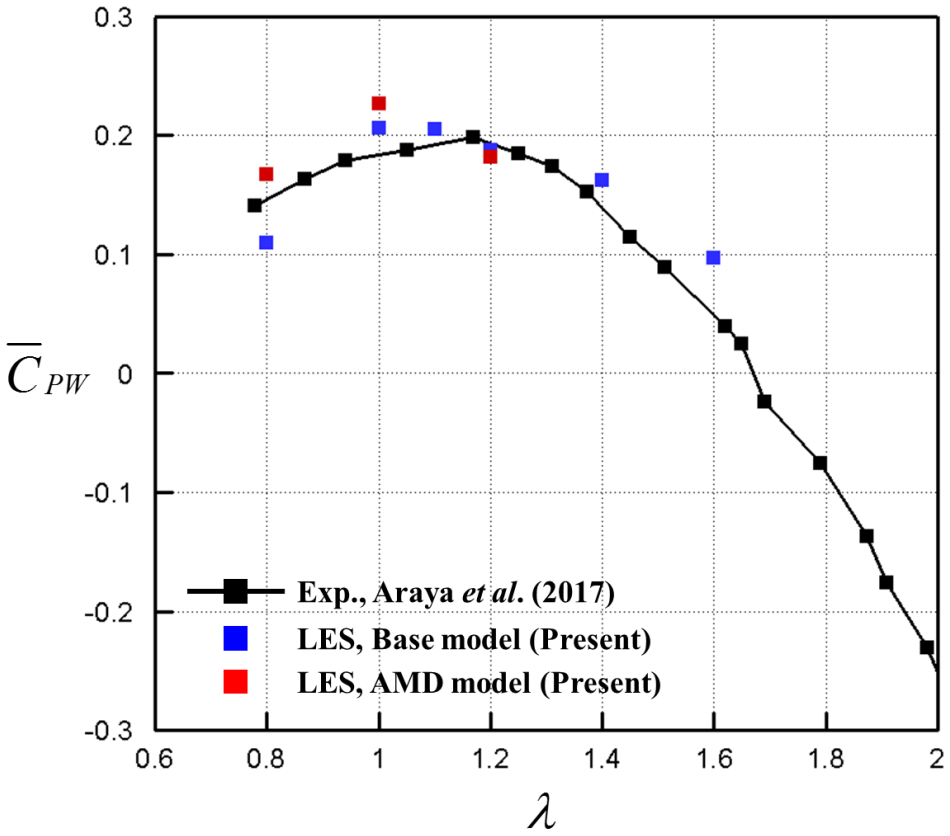

FIGURE 4.2 Performances of the base and AMD models.

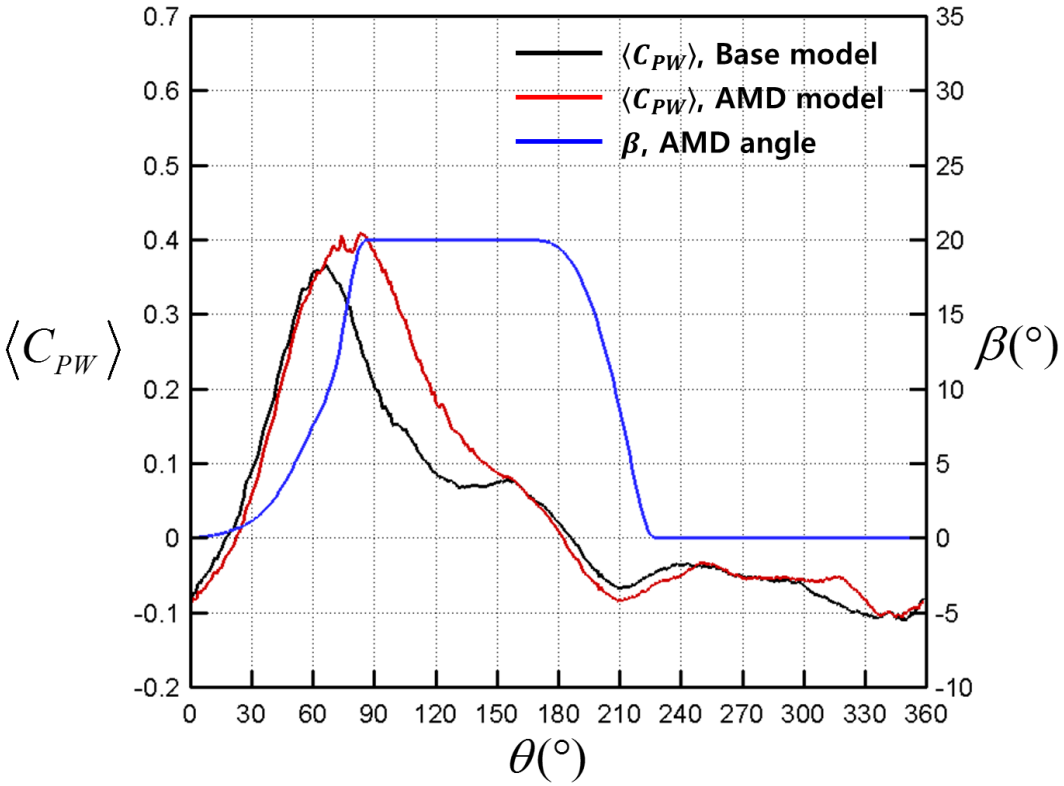

FIGURE 4.3 Azimuthal variations of phase-averaged power coefficients for one blade and the AMD angle at λ = 0.8.

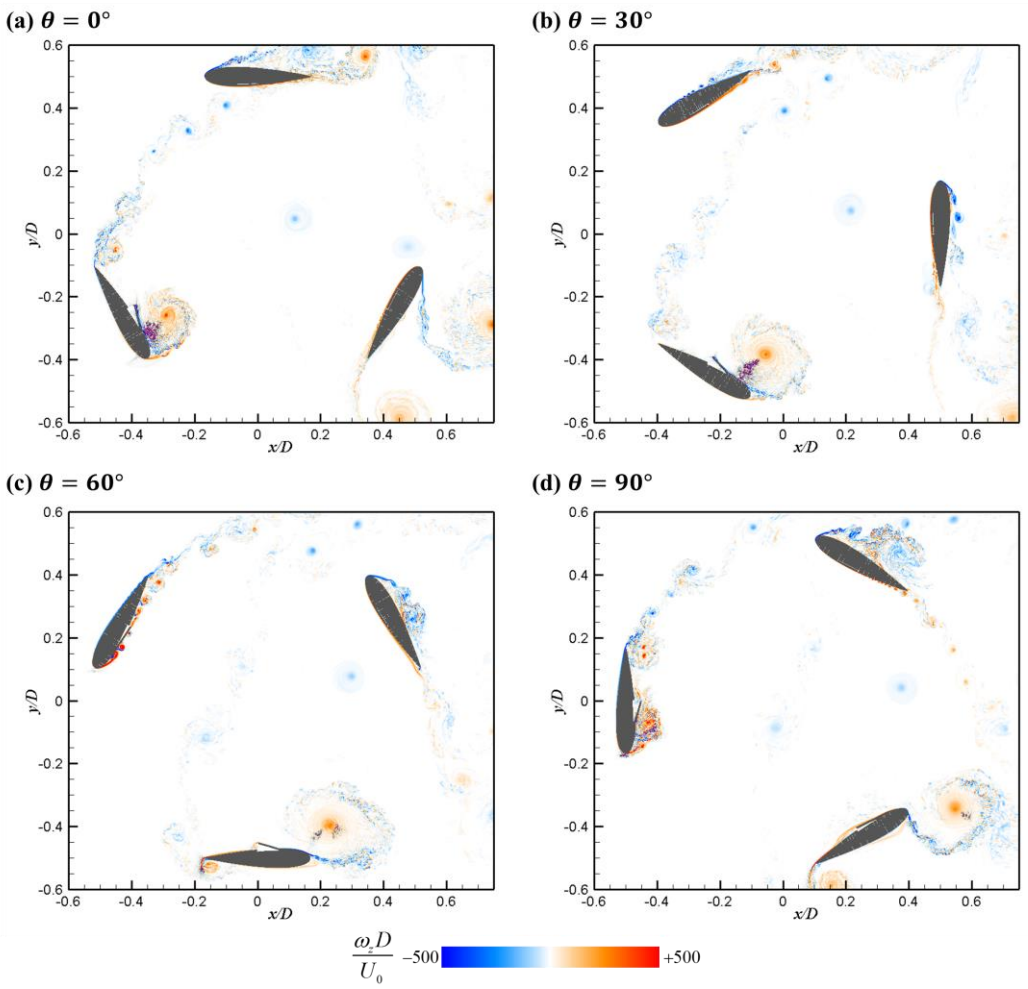

FIGURE 4.4 Contours of the instantaneous spanwise vorticity for the AMD model at λ = 0.8: (a) θ = 0°; (b) θ = 30°; (c) θ = 60°; (d) θ = 90°.

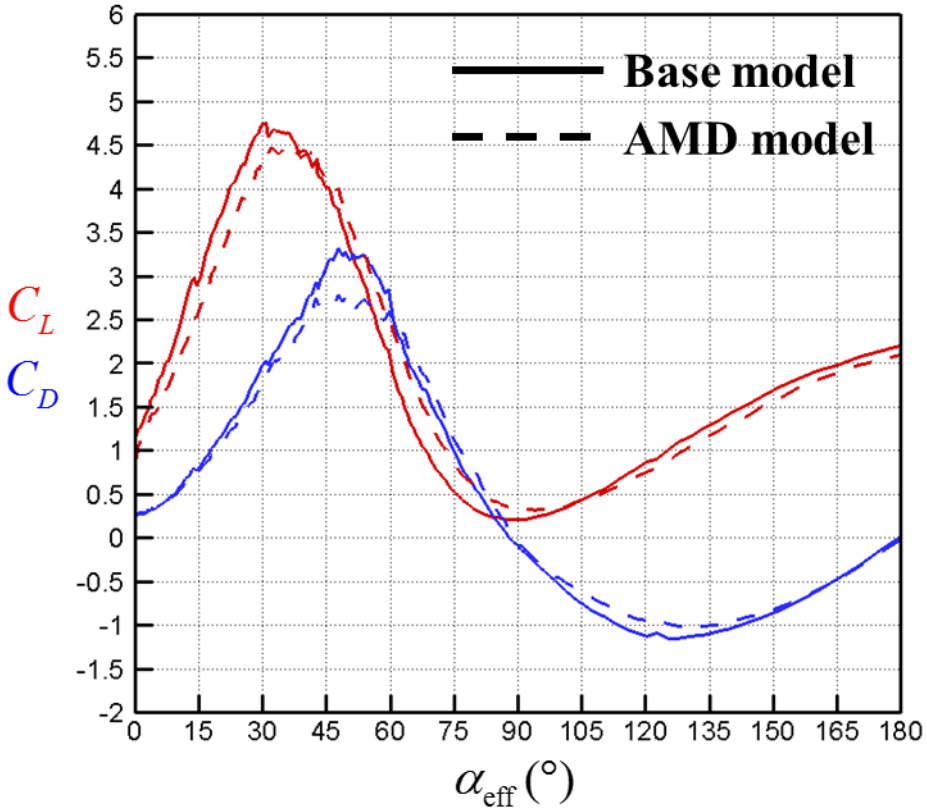

FIGURE 4.5 Variations of lift (red) and drag (blue) coefficients with the effective angle of attack in the upwind region at λ = 0.8.

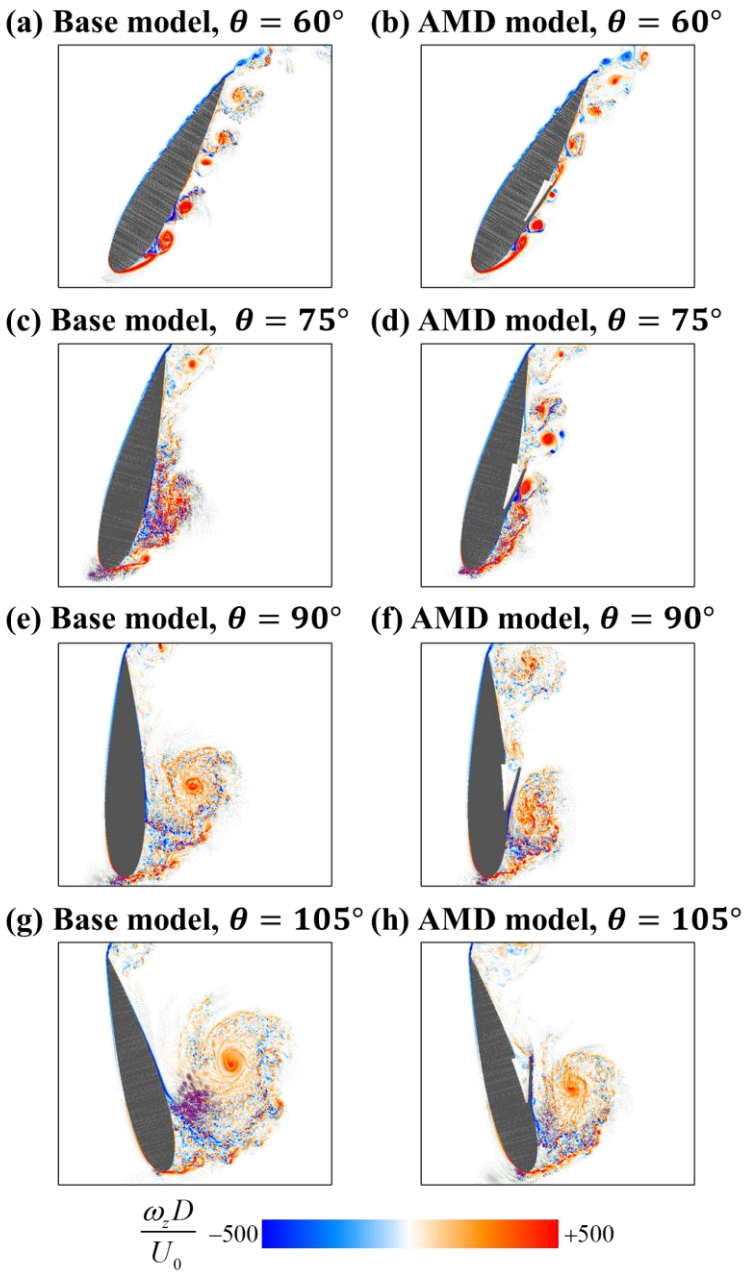

FIGURE 4.6 Instantaneous spanwise vorticity contours around the blade in the upwind region at λ = 0.8: (a, c, e, g) base model; (b, d, f, h) AMD model; (a, b) θ = 60°; (c, d) θ = 75°; (e, f) θ = 90°; (g, h) θ = 105°.

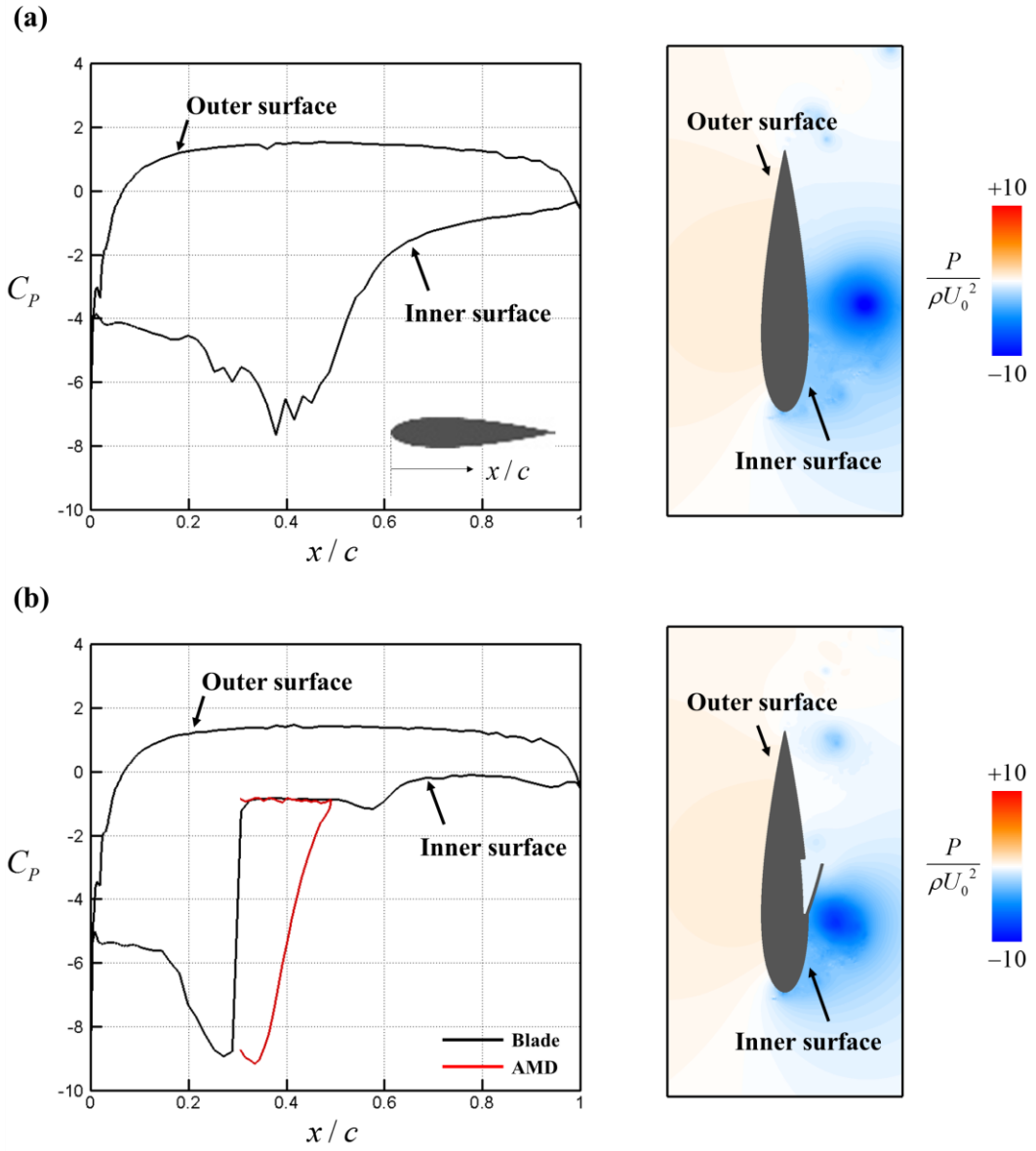

FIGURE 4.7 Pressure distribution on the blade surface and instantaneous pressure contours at $\theta = 90^{o}$ for $\lambda = 0.8$: (a) base model; (b) AMD model.

Summary and Conclusion

We conducted large eddy simulations to analyze the flow around the three-blade VAWT and the unsteady aerodynamics of the blades and applied the AMD to the blades to enhance the performance of the VAWT. We verified the performance of the VAWT according to the tip speed ratio, and the variation of the power coefficient along the azimuthal position of the blade was investigated at the optimal tip speed ratio. As the blade rotated, positive and negative powers were generated in the upwind and downwind regions, respectively. We divided the rotating region into three regions based on the variation of the power: the upwind region A (power increasing), upwind region B (power decreasing), and downwind region.

As the blade rotated, various flow phenomena occurred: flow separation, vortex shedding, and wake interference. In the upwind region A, the flow was nearly attached around the blade, and the lift coefficient increased larger than the drag coefficient as the effective angle of attack increased. After the effective angle of attack exceeded the stall angle in the upwind region B, the flow separation and the leading edge vortex formation occurred at the leading edge, and the lift coefficient decreased rapidly. In the downwind region, the lift and drag changed very mildly although the effective angle of attack changed and the flow separation occurred, which might be because the blade passed through the wake from the preceding blade.

We applied the AMD to the inner surface of the blade to suppress the flow separation in the upwind region. The AMD popped up rapidly when the flow separation occurred in the upwind region B, and then it closed as the flow was attached on the inner surface of the blade in the downwind region. When the AMD opened, the flow separation was suppressed and the shedding of leading edge vortex was delayed, which caused the drag reduction during dynamic stall. Consequently, the time-averaged power coefficients were enhanced at $\lambda = 0.8$ and $\lambda = 1$.

References

Araya, D. B., Colonius, T., & Dabiri, J. O., 2017, Transition to bluff-body dynamics in the wake of vertical-axis wind turbines, *Journal of Fluid Mechanics*, **813**, 346-381.

Bechert, D. W., Bruse, M., Hage, W., & Meyer, R., 1997, Biological Surfaces and their Technological Application – Laboratory and Flight Experiments on Drag Reduction and Separation Control, *AIAA Paper*, 97-1960.

Bhutta, M. M. A., Hayat, N., Farooq, A. U., Ali, Z., Jamil, S. R., & Hussain, Z., 2012, Vertical axis wind turbine – A review of various configurations and design techniques, *Renewable & Sustainable Energy Reviews*, **16**(4), 1926-1939.

Buchner, A. J., Soria, J., Honnery, D., & Smits, A. J., 2018, Dynamic stall in vertical axis wind turbines: scaling and topological considerations, *Journal of Fluid Mechanics*, **841**, 746-766.

Choi, H., & Moin, P., 1994, Effects of the Computational Time-Step on Numerical-Solutions of Turbulent-Flow, *Journal of Computational Physics*, **113**(1), 1-4.

Corke, T. C., & Thomas, F. O., 2015, Dynamic stall in Pitching Airfoils: Aerodynamic Damping and Compressibility Effects, *Annual Review of Fluid Mechanics*, **47**, 479-505.

Dabiri, J. O., 2011, Potential order-of-magnitude enhancement of wind farm power density via counter-rotating vertical axis wind turbine arrays, *Journal of Renewable and Sustainable Energy*, **3**(4), 043104.

Dominy, R., Lunt, P., Bickerdyke, A., & Domniny, I., Self-starting capability of a Darrieus turbine, *Proceedings of the Institution of Mechanical Engineers Part A – Journal of Power and Energy*, **221**(1), 111-120.

Ferreira, C. S., van Kuik, G., van Bussel, G., & Scarano, F., 2009, Visualization by PIV of dynamic stall on a vertical axis wind turbine, *Experiments in Fluids*, **46**(1), 97-108.

Frunzulica, F., Dumitrache, A., & Suatean, B., 2014, Numerical investigations of passive flow control elements for vertical axis wind turbine, *AIP Conference Proceedings*, **1637**, 331-340.

Fujisawa, N., & Takeuchi, M., 1999, Flow Visualization and PIV Measurement of Flow

Field around a Darrieus Rotor in Dynamic stall, *Journal of Visualization*, **1**(4), 379-386.

Hezaveh, S. H., Bou-Zeid, E., Lohry, M. W., & Martinelli, L., 2017, Simulation and wake analysis of a single vertical axis wind turbine, *Wind Energy*, **20**(4), 713-730.

Hill, N., Dominy, R., Ingram, G., & Dominy, J., 2009, Darrieus turbines: the physics of self-starting, *Proceedings of the Institution of Mechanical Engineers Part A – Journal of Power and Energy*, **223**(1), 21-29.

Howell, R., Qin, N., Edwards, J., & Durrani, N., 2010, Wind tunnel and numerical study of a small vertical axis wind turbine, *Renewable Energy*, **35**(2), 412-422.

Islam, M., Ting, D. S. K., & Fartaj, A., 2008, Aerodynamic models for Darrieus-type straight-bladed vertical axis wind turbines, *Renewable & Sustainable Energy Reviews*, **12**(4), 1087-1109.

Kernstine, K. H., Moore, C. J., Cutler, A., & Mittal, R., 2008, Initial Characterization of Self-Activated Movable Flaps, "Pop-Up Feathers", *AIAA Paper*, 2008-0369.

Kim, D., Lee, H., Yi, W., & Choi, H., 2016, A bio-inspired device for drag reduction on a three-dimensional model vehicle, *Bioinspiration & Biomimetics*, **11**(2), 026004.

Kim, J., Kim, D., & Choi, H., 2001, An immersed-boundary finite-volume method for simulations of flow in complex geometries, *Journal of Computational Physics*, **171**(1), 132-150.

Kim, K., Baek, S. J., & Sung, H. J., 2002, An implicit velocity decoupling procedure for the incompressible Navier-Stokes equations, *International Journal for Numerical Methods in Fluids*, **38**(2), 125-138.

Kirke, B., 1998, Evaluation of self-starting vertical axis wind turbines for stand-alone applications, PhD Thesis, Griffith University, Faculty of Engineering and Information Technology, School of Engineering, Australia.

Lee, J., Choi, H., & Park, N., 2010, Dynamic global model for large eddy simulation of transient flow, *Physics of Fluids*, **22**(7), 075106.

Li, C., Xiao, Y. Q., Xu, Y. L., Peng, Y. X., Hu, G., & Zhu, S. Y., 2018, Optimization of blade pitch in H-rotor vertical axis wind turbines through computational fluid dynamics simulations, *Applied Energy*, **212**, 1107-1125.

Liebe, W., 1979, Der auftrieb am tragflügel: Entstehung und zusammenbruch, *Aerokurier*, **12**, 1520-1523.

Marsh, P., Ranmuthugala, D., Penesis, I., & Thomas, G., 2015, Three-dimensional numerical simulations of straight-bladed vertical axis tidal turbines investigating power output, torque ripple and mounting forces, *Renewable Energy*, **83**, 67-77.

McLaren, K., Tullis, S., & Ziada, S., 2012, Computational fluid dynamics simulation of the aerodynamics of a high solidity, small-scale vertical axis wind turbine, *Wind Energy*, **15**(3), 349-361.

Meyer, R., Hage, W., Bechert, D. W., Schatz, M., Knacke, T., & Thiele, F., 2007, Separation control by self-activated movable flaps, *AIAA Journal*, **45**(1), 191-199.

Ouro, P., & Stoesser, T., 2017, An immersed boundary-based large-eddy simulation approach to predict the performance of vertical axis tidal turbines, *Computers & Fluids*, **152**, 74-87.

Park, N., Lee, S., Lee, J., & Choi, H., 2006, A dynamic subgrid-scale eddy viscosity model with a global model coefficient, *Physics of Fluids*, **18**(12), 125109.

Pope, K., Dincer, I., & Naterer, G. F., 2010, Energy and exergy efficiency comparison of horizontal and vertical axis wind turbines, *Renewable energy*, **35**, 2102-2113.

Posa, A., & Balaras, E., 2018, Large Eddy Simulation of an isolated vertical axis wind turbine, *Journal of Wind Engineering and Industrial Aerodynamics*, **172**, 139-151.

Posa, A., Parker, C. M., Leftwich, M. C., & Balaras, E., 2016, Wake structure of a single vertical axis wind turbine, *International Journal of Heat and Fluid Flow*, **61**, 75-84.

Rechenberg, I., Bannasch, R., Patone, G., & Müller, W., 1995, Aeroflexible Oberflächenklappen als "Rückstrombremsen" nach dem Vorbild der Deckfedern des Vogelflügels, Statusbericht 1995 für das BMBF-Vorhaben 13N6536, Inst. f. Bionik u. Evolutionstechnik, TU Berlin.

Sobhani, E., Ghaffari, M., & Maghrebi, M. J., 2017, Numerical investigation of dimple effects on Darrieus vertical axis wind turbine, *Energy*, **133**, 231-241.

Tsai, H. C., & Colonius, T., 2016, Numerical Investigation of Self-starting Capability of Vertical-Axis Wind Turbines at Low Reynolds Numbers, 34th AIAA Applied

Aerodynamics Conference, Washington, D. C., 1-12.

Untaroiu, A., Wood, H. G., Allaire, P. E., & Ribando, R. J., 2011, Investigation of Self-Starting Capability of Vertical Axis Wind Turbines Using a Computational Fluid Dynamics Approach, *Journal of Solar Energy Engineering*, **133**(4), 041010.

Wang, C. H. J., & Schlüter, J., 2012, Stall control with feathers: Self-activated flaps on finite wings at low Reynolds numbers, *Comptes Rendus Mecanique*, **340**, 57-66.

Wang, Z. Y., & Zhuang, M., 2017, Leading-edge serrations for performance improvement on a vertical-axis wind turbine at low tip-speed-ratios, *Applied Energy*, **208**, 1184-1197.

Yang, Y., Li, C., Zhang, W. F., Guo, X. Y., & Yuan, Q. Y., 2017, Investigation on aerodynamics and active flow control of a vertical axis wind turbine with flapped airfoil, *Journal of Mechanical Science and Technology*, **31**(4), 1645-1655.

수직축 풍력발전기 주위 유동에 관한 수치 해석 연구 및 자동 디플렉터를 이용한 유동 제어

서울대학교 대학원

기계항공공학부

김형민

요약

본 연구에서는 수직축 풍력발전기 회전익 주변의 유동 및 공력성능을 분석하기 위해 주 유동 속도와 회전 직경을 기준으로 한 레이놀즈 수 80,000에서 큰 에디 모사 시뮬레이션을 수행하였다. Tip speed ratio에 따른 수직축 풍력발전기의 효율 변화를 검증하고, 최적 tip speed ratio에서 회전익 위치에 따른 공력성능 특성을 분석하였다. 상류지역에서 회전익의 받음각이 증가함에 따라 회전익의 양력이 항력보다 크게 상승하다가, 주변에서 유동박리와 와류발생이 일어나고 동적 실속이 발생하여 양력이 크게 감소하게 된다. 반면, 하류지역에서는 유동 변화에도 불구하고 회전익의 공력성능의 변화가 거의 일어나지 않는다. 상류지역에서 동적 실속이 일어날 때 회전익의 공력성능을 향상시키기 위해

automatic moving deflector (AMD)를 적용하였다. 동적 실속 과정에서 AMD는 유동에 의해 자동으로 열리게 닫히게 되고, AMD가 열릴 때 유동박리와 와류 발생이 억제됨에 따라 항력이 감소하는 것을 확인하였다. 결과적으로 수직축 풍력발전기의 효율은 tip speed ratio가 0.8과 1일 때 향상되는 것을 확인하였다.

주요어: 수직축 풍력발전기, 동적 실속, 생체모방 유동제어, 자동 디플렉터

학번: 2017-24571